



## Multi-isotopic and trace element evidence against different formation pathways for oyster microstructures

Niels J. de Winter<sup>a,b,\*</sup>, Linda K. Dämmer<sup>c,d</sup>, Michaela Falkenroth<sup>c,d,e</sup>,  
Gert-Jan Reichart<sup>a,c</sup>, Simone Moretti<sup>f</sup>, Alfredo Martínez-García<sup>f</sup>, Nils Höche<sup>g</sup>,  
Bernd R. Schöne<sup>g</sup>, Katerina Rodiouchkina<sup>h</sup>, Steven Goderis<sup>b</sup>, Frank Vanhaecke<sup>h</sup>,  
Sonja M. van Leeuwen<sup>i</sup>, Martin Ziegler<sup>a</sup>

<sup>a</sup> Dept. of Earth Sciences, Utrecht University, Utrecht, the Netherlands

<sup>b</sup> AMGC Research Group, Vrije Universiteit Brussel, Brussels, Belgium

<sup>c</sup> Ocean Systems Department, Royal Netherlands Institute for Sea Research, Texel, the Netherlands

<sup>d</sup> Environmental Geology, Department of Geology, Institute of Geosciences, University of Bonn, Bonn, Germany

<sup>e</sup> Neotectonics and Natural Hazards Research Group, Rheinisch-Westfälische Technische Hochschule Aachen, Aachen, Germany

<sup>f</sup> Max Planck Institute for Chemistry, Otto Hahn Institute, Mainz, Germany

<sup>g</sup> Institute of Geosciences, University of Mainz, Mainz, Germany

<sup>h</sup> Atomic and Mass Spectrometry - A&MS Research Group, Department of Chemistry, Ghent University, Ghent, Belgium

<sup>i</sup> Coastal Systems Department, Royal Netherlands Institute for Sea Research, Texel, the Netherlands

Received 10 August 2020; accepted in revised form 7 June 2021; Available online 15 June 2021

### Abstract

Shells of oysters (Ostreidae) are predominantly composed of foliated and chalky calcite microstructures. The formation process of the more porous chalky structure is subject to debate, with some studies suggesting that it is not formed directly by the oyster but rather through microbial mineralization within the shell. Here, this hypothesis is tested in modern shells of the Pacific oyster (*Crassostrea gigas*) from coastal regions in France and the Netherlands. We combine measurements of stable carbon, oxygen, nitrogen, sulfur, and clumped isotope ratios with high-resolution spatially resolved element (Na, Mg, Cl, S, Mn and Sr) data and microscopic observations of chalky and foliated microstructures in the oyster shells. Our results show no isotopic differences between the different microstructures, arguing against formation of the chalky calcite by microorganisms. However, we observe a small difference in the oxygen isotope ratio (0.32‰) and clumped isotope composition (0.017‰) between the microstructures, which is likely caused by sampling biases due to seasonal differences in growth rate and the short timespan over which the chalky microstructure forms. We therefore recommend sampling profiles through the foliated microstructure to control for strong seasonal variability recorded in the shell which can bias environmental reconstructions. High-resolution (25–50 μm) Na, Mg, Cl, S, Mn and Sr profiles yield empirical distribution coefficients between seawater and shell calcite for these elements. Significant differences in element concentrations and distribution coefficients were confirmed between the two microstructures, likely reflecting differences in mineralization rates or inclusion of non-lattice-bound elements. Only Mg/Ca ratios in the foliated microstructure vary predictably with growth seasonality, and we show that these can be used to establish accurate oyster shell chronologies. The observed effect of mineralization rate on element incorporation into oyster shells should be considered while developing potential element proxies for paleoclimate reconstructions. Trace element proxies in oyster shells should be interpreted with caution, especially when element chemical properties were measured in different microstructures.

\* Corresponding author at: Dept. of Earth Sciences, Utrecht University, Utrecht, the Netherlands.  
E-mail addresses: [nidewint@vub.be](mailto:nidewint@vub.be), [n.j.dewinter@uu.nl](mailto:n.j.dewinter@uu.nl) (N.J. de Winter).

© 2021 The Author(s). Published by Elsevier Ltd. This is an open access article under the CC BY license (<http://creativecommons.org/licenses/by/4.0/>).

**Keywords:** Oyster; Bivalve; trace element; Stable isotope; microstructure; Sclerochronology; Mg/Ca; Clumped isotopes; nitrogen isotopes; Sulfur isotopes; *Crassostrea gigas*; SEM; XRF; Calcite; Biomineralization; Distribution coefficient; Paleoclimate

## 1. INTRODUCTION

Oysters (Ostreidae) are a highly diverse and specialized group of bivalves that live cemented to hard substrates, predominantly in shallow marine environments (Yonge, 1960). Oysters have obtained a widespread distribution and inhabit a diverse set of environments, from fully marine habitats to turbid brackish estuaries (Carriker, 1951; Huber, 2010; Do Amaral and Simone, 2014). As reef builders, many oyster taxa are keystone species in shallow marine environments (Newell, 1988; Grabowski and Peterson, 2007; Scyphers et al., 2011; Grabowski et al., 2012). Furthermore, oyster reefs play a vital role in local chemical cycles due to their high population density and highly efficient filtration (Dame et al., 1984; Dame, 1999; zu Ermgassen et al., 2013). The formation, structure and chemistry of oyster shells is of interest because their composite shell structures have attractive (mechanical) properties which have various industrial applications (Addadi et al., 2006; Cranford and Buehler, 2010; Luz and Mano, 2010) and because oyster shells serve as high-resolution archives for past climates and environments (Surge and Lohmann, 2008; Ullmann et al., 2010; Mouchi et al., 2013; Bougeois et al., 2018; de Winter et al., 2018; 2020a).

Many oysters grow thick, irregular shells predominantly consisting of two different calcite microstructures. The “foliated” calcite consists of densely packed, foliated calcite laths while the “chalky” calcite (Gray, 1833) is composed of more loosely and chaotically organized blades surrounded by interconnected pores (Carriker et al., 1980; Checa et al., 2007). Other mineralized structures include smaller volumes of prismatic calcite on the adductor muscle scar and shell margins (e.g., in *Crassostrea virginica*) and minor amounts of aragonite fortifying the resilium (Carriker et al., 1980). The presence of the chalky structure in the form of lenses between the foliated calcite is typical of the Ostreidae family and its process of formation is highly debated. This has recently spurred researchers to investigate the chemical (Surge et al., 2001; Ullmann et al., 2010; 2013; Mouchi et al., 2016), microstructural (Lee et al., 2011; Checa et al., 2018; Banker and Sumner, 2020) and physiological (Higuera-Ruiz and Elorza, 2009) differences between chalky and foliated structures and their organic matrices. Some authors suggest that the chalky structure may be formed through “remote mineralization” by sulfur-reducing bacteria living within shell vesicles (Chinzei and Seilacher, 1993; Vermeij, 2014). Others, however, have challenged this hypothesis by suggesting the structural difference results from local detachment of the mantle from the forming shell. This would serve as a

mechanism to accommodate the typical plasticity of shell shape allowing oysters to attach to rough substrates and adapt to space limitations during growth (Checa et al., 2018; Banker and Sumner, 2020). This distinction has important implications both for understanding the formation pathway of these biomineralized structures and for the interpretation of the chemistry of oyster shell calcite for environmental monitoring and paleoclimate reconstruction.

While some authors have reported chemical and isotopic differences between oyster microstructures, for example, in their elemental composition (e.g. Higuera-Ruiz and Elorza, 2009; Ullmann et al., 2010; 2013), the origin of these differences is poorly understood because these studies lack characterization of the differences in key isotopic systems (e.g. nitrogen and sulfur isotope ratios) or a precise link between shell chemistry and the chemistry of the growth environment of the animal. The strong isotope fractionation associated with microbial sulfur reduction (Brunner et al., 2005; Jia et al., 2015; Mouchi et al., 2016) and the large differences in element partitioning between eukaryotic and microbial carbonates (e.g. McGenity and Sellwood, 1999; Webb and Kamber, 2000; Terakado et al., 2010) may provide conclusive evidence for or against the “remote mineralization” hypothesis in the chemical and isotopic signatures of the respective microstructures. If the chalky shell structures in oysters were formed by sulfur reducing microbes (the “remote mineralization” hypothesis), a large difference in both isotope and element composition is expected.

Here, we combine multiple stable isotope ratio ( $\delta^{13}\text{C}_c$ ,  $\delta^{15}\text{N}$  and  $\delta^{34}\text{S}$ ) analyses from both chalky and foliated microstructures in the Pacific oyster *Crassostrea gigas* (Thunberg, 1793; syn. *Magallana gigas*) with *in situ* trace element records to refute the “remote mineralization” hypothesis in modern oysters. In addition to this multiproxy dataset, we present stable oxygen ( $\delta^{18}\text{O}_c$ ) and clumped isotope ( $\Delta_{47}$ ) values of the carbonate in the microstructures. As common proxies for paleotemperature, we assess whether  $\delta^{18}\text{O}_c$  and  $\Delta_{47}$  values in both microstructures reliably record the temperature and isotopic composition of the seawater ( $\delta^{18}\text{O}_w$ ) and can be used for climate reconstructions. We use high-resolution Mg/Ca profiles through the shells to assess the timing of growth and discuss whether microstructure formation is seasonally controlled. Finally, we evaluate the empirical distribution coefficients of Na, Mg, Cl, S, Mn and Sr into the chalky and foliated microstructure of *C. gigas*, to quantify chemical differences between the microstructures, assess the effect of growth rate on shell chemistry and evaluate the potential use of element records for environmental reconstructions.

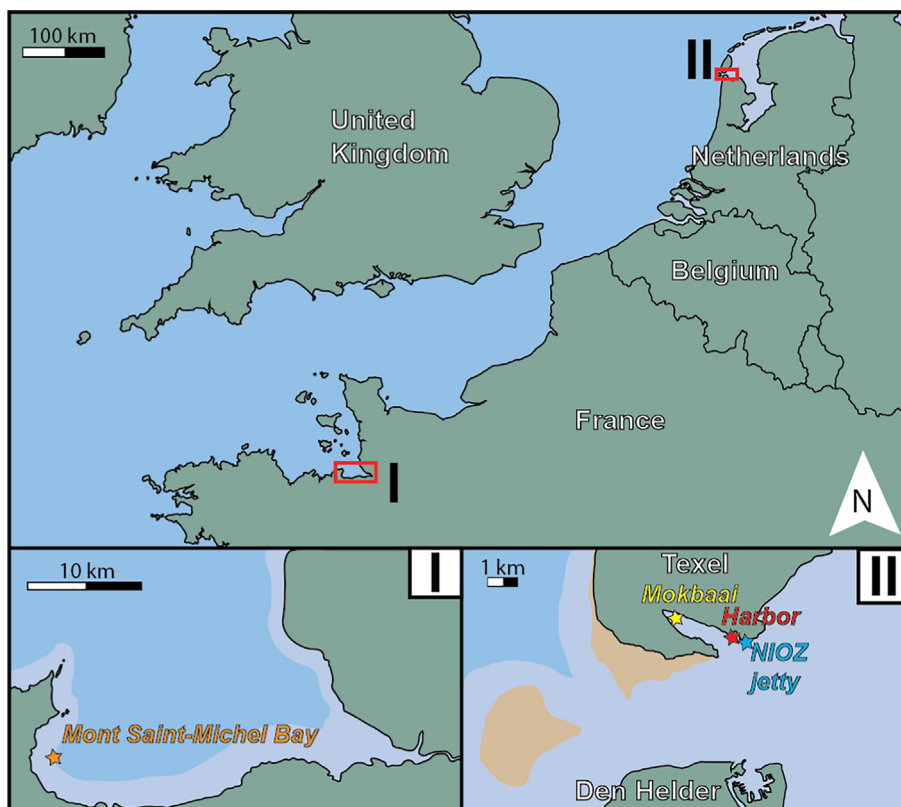


Fig. 1. Overview of the three localities where the specimens of *C. gigas* used in this study were acquired. Star-shaped symbols highlight the sampling sites of specimens **O1-8** from Brittany (France, in orange), **M1-6** from the Mokbaai (the Netherlands, in yellow) and **H1-4** from TESO Harbor (NL, in red). The jetty of NIOZ where in situ temperature and salinity measurements were taken is indicated in blue. Light blue colors indicate areas that are subaerially exposed during low tide, while brown colors indicate moving sand banks.

## 2. MATERIALS AND METHODS

### 2.1. Sample acquisition

A total of 18 specimens of *C. gigas* were collected from three different localities (see Fig. 1). Eight specimens (hereafter: **O1-8**) were obtained from a cultivation area in coastal Brittany (France, 49°04.00' N, 001°35.47' W; hereafter “**BR**”) where they were grown at an average water depth of 5–10 meters. The bivalves were harvested on February 14th, 2017. Six specimens were collected in the Mokbaai, a tidal inlet located in the protected National Park Duinen van Texel at the southern coast of the island Texel in the Wadden Sea in the northwest of the Netherlands (53°00.90' N, 004°45.20' W, hereafter “**MB**”). Two of these specimens (hereafter: **M1** and **M2**) were collected during a first sampling campaign on July 6th, 2017 and four additional specimens (**M3-6**) were collected during a second campaign on July 5th, 2018. Four specimens were collected from the harbor of the TESO ferry at the southern coast of Texel (53°00.10' N, 004°46.20' W, hereafter “**TH**”). Two of these specimens (hereafter: **H1** and **H2**) were collected during a first sampling campaign on July 6th, 2017 and two additional specimens (**H3** and **H4**) were collected during a second campaign on July 5th, 2018.

### 2.2. Sample preparation

The convex left valves of the shells were superficially cleaned to remove algae and other contaminants using a soft brush and an ultrasonic bath. They were disinfected using acetone ( $C_3H_5OH$ ) and distilled water, and oven dried overnight at 50 °C. Left valves were chosen in this study because they are larger, contain relatively low amounts of aragonite in oysters, and have better developed hinges (see Kennedy et al., 1996; Surge et al., 2001). This provides more surface area for measurement, allows growth features to be more readily recognized and permits a higher sampling resolution. Shell valves were sectioned dorsoventrally along their axis of maximum growth (following Surge et al., 2001) using a slow rotating saw with a diamond coated blade (thickness = 1 mm). Cross-sections were placed such that the most recently formed shell material was exposed. From the larger shells from Texel (**M1-4**, **H1-4**), the hinge plate was isolated for easier handling. The cross-sections of all samples were polished using silicon carbide polishing disks (up to P2400 grit size). Polished samples were imaged by means of color scanning (RGB) using an Epson® 1850 flatbed scanner (Seiko Epson Corp., Nagano, Japan) at a pixel resolution of 6400 dpi ( $\pm 4 \mu m$  pixel size; see Fig. 2). The opposing sides of the cross-

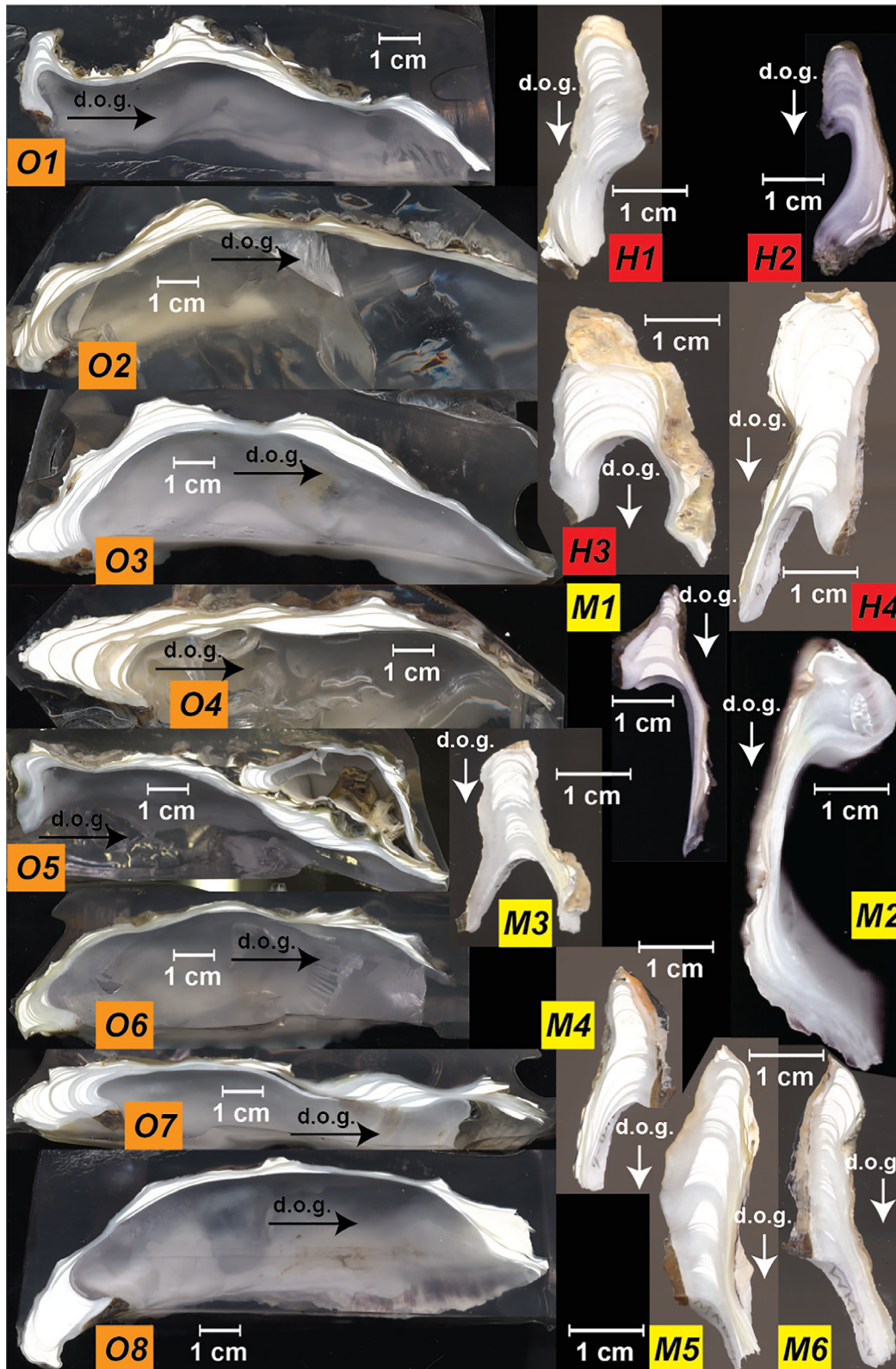


Fig. 2. Overview of color scans taken of cross-sections through the entire shell (O1-8, in orange) or hinge region (H1-4, in red, and M1-6, in yellow). Arrows labeled “d.o.g.” indicate direction of growth.

section through the shell hinge of selected specimens (**O2**, **O6**, **O7**, **O8**, **M2**, **M5** and **H1**) were cut parallel to the growth axis and mounted on glass slides to produce thick sections for microscopy. These thick sections were polished using a 1.00, 0.30 and 0.05  $\mu\text{m}$   $\text{Al}_2\text{O}_3$  suspension. Polished thick sections were treated with Mutvei's solution, a reagent that etches the surface, fixes organic compounds and stains mucopolysaccharides, which aids in identifying micro-growth patterns (Schöne et al., 2005a). The sections were immersed in Mutvei's solution which was held at 38 °C for 20 minutes under constant stirring until properly stained.

### 2.3. Microscopy

Polished thick sections were imaged both before and after Mutvei staining using a stereomicroscope with sectoral dark field illumination at 30  $\times$  magnification. Images were taken covering the full polished surface of the hinge using a Canon EOS 550D camera and stitched together into a microscopic composite using the image processing software ImageJ/Fiji (Schindelin et al., 2012; see reduced-quality versions in Fig. 3A–B and full quality versions in [Supplementary Information](#)). Thick sections of specimens **O2**, **O6** and **O7** were then mounted on a Scanning Electron Microscope (SEM) stub with adhesive carbon stickers and sputtered with a 4–5 nm thick platinum layer. Images were taken using a LOT Quantum Design Phenom PRO Desktop SEM (Quantum Design GmbH, Grimbergen, Belgium; third generation) equipped with a  $\text{CeBr}_6$  source and backscatter electron detector operating at a voltage of 10 kV and a working distance (distance between pole piece and sample) of ca. 5.5 mm (following Höche et al., 2020). SEM magnifications varied between 200 $\times$  and 16000 $\times$ . Full quality versions of SEM micrographs are provided in [Supplementary Information](#).

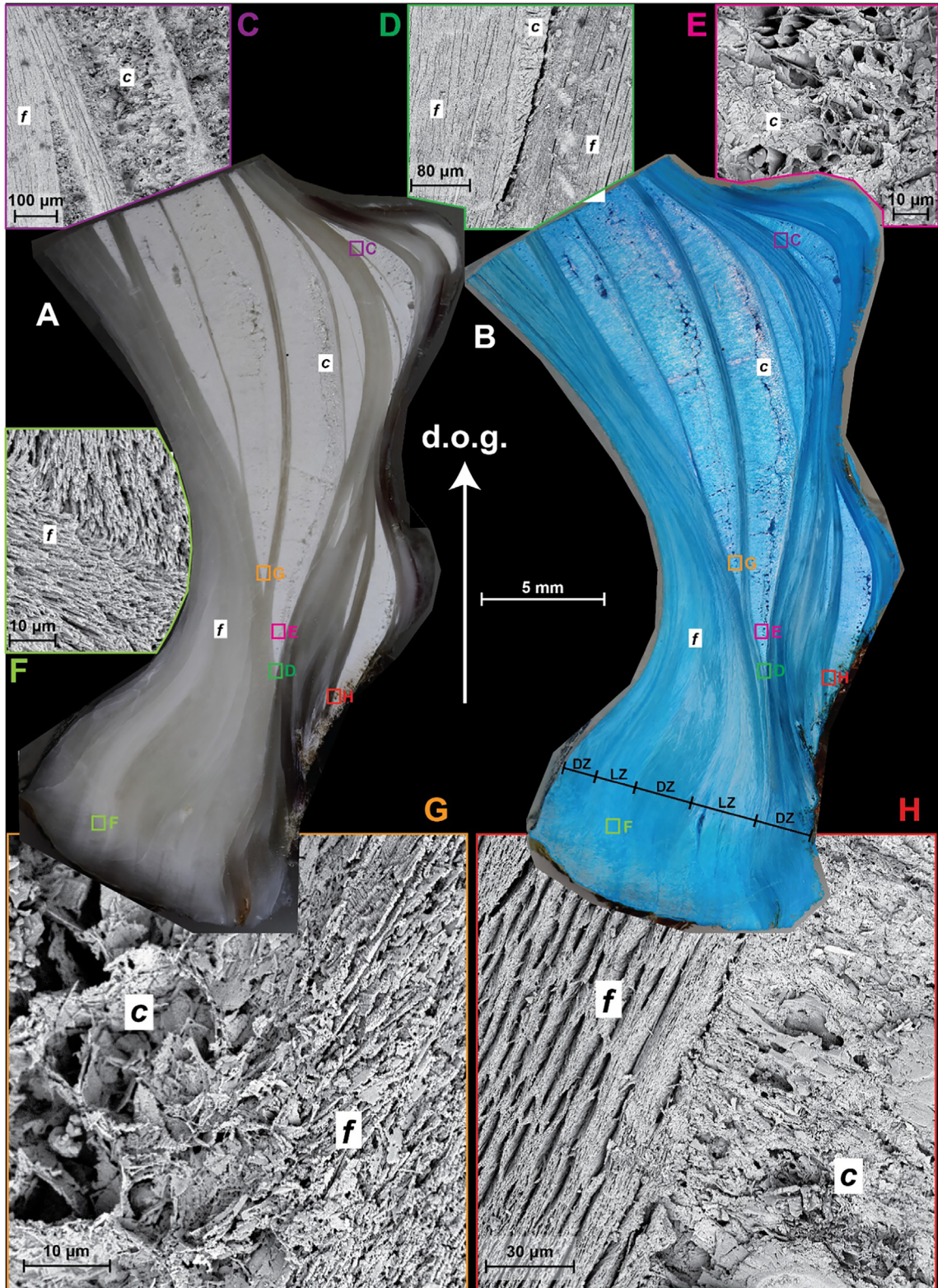
### 2.4. X-ray fluorescence spectrometry

Elemental concentrations were measured *in situ* in the hinge region on the polished cross-sections using a Bruker® M4 Tornado micro-X-ray Fluorescence scanner (Bruker nano GmbH, Berlin, Germany) equipped with a Rh X-Ray source using maximum energy settings (50 kV, 600  $\mu\text{A}$ ) with a spot size of 25  $\mu\text{m}$  (Mo  $\text{K}\alpha$ ) and two Silicon Drift detectors. The XRF setup is described in detail in de Winter and Claeys (2016). Quantitative XRF element profiles were obtained for all polished cross-sections using two measurement strategies (see Fig. 4): First, a profile was measured in the direction of maximum growth through the hinge of the shell in cross-section, perpendicular to the growth bands and crossing foliated and chalky calcite layers (as in Surge et al., 2001; Ullmann et al., 2010; 2013). Second, a profile was measured perpendicular to the growth lines, exclusively sampling the dense foliated calcite layers in the hinge of the shell (as in Surge and Lohmann, 2008; Mouchi et al., 2013; Durham et al., 2017). The position of the profiles is indicated in [Supplementary Information](#). All element profiles were measured using the point-by-point line scanning method outlined in de Winter et al.

(2017a). An integration time of 60 s per point and the sampling density (20–40 analyses/mm, variable between individuals) were chosen as a compromise between obtaining high-resolution profiles and achieving sufficient count statistics for the instrument to reach the Time of Stable Reproducibility (TSR) providing reproducible concentrations for the elements of interest (de Winter et al., 2017b). All XRF line scans were quantified using the Bruker Esprit® fundamental parameters (FP) quantification relative to the BAS CRM 393 limestone standard (Bureau of Analyzed Samples, Middlesbrough, UK; BAS) and calibrated using a range of certified carbonate reference materials: CCH-1 (Université de Liège, Belgium), COQ-1 (US Geological Survey, Denver, CO, USA), CRM393 (BAS), CRM512 (BAS), CRM513 (BAS), ECRM782 (BAS) and SRM-1d (National Institute of Standards and Technology, Gaithersburg, MD, USA).  $R^2$  values of calibration curves through certified concentrations of these reference materials exceeded 0.99 and reproducibility standard deviations of repeated measurements on the same homogenous reference material were better than 10 % relative to the mean. The effects of varying porosity through the shell on XRF results were tested by monitoring Ca concentration as internal standard, and datapoints with Ca concentrations deviating more than 2 wt% from the reference Ca concentration in carbonates of 38.5 wt% were not used. The discussion of element profiles is limited to the concentrations of sodium (Na), magnesium (Mg), sulfur (S), chlorine (Cl), calcium (Ca), manganese (Mn) and strontium (Sr). Due to the low energy of X-rays fluorescing off Na and the relative scarcity of carbonate reference materials with certified Cl concentrations, calibration lines for these elements were less robust. However, high-resolution profiles provided many datapoints in each microstructure and exhibit robust trends of Na and Cl concentrations through the shells. Note that the XRF excitation volume includes the concentration of elements regardless of their hosting within the biomineral, resulting in weighted mean concentrations of elements within the entire biomineral, both within and outside the calcite lattice. Uncertainties on mean trace element concentrations of microstructures were calculated at the 95 % confidence level from variability of all datapoints within the microstructure of each specimen to include both measurement uncertainty and variability within the microstructure. Raw data of  $\mu\text{XRF}$  analyses are provided in the [Supplementary Information](#).

### 2.5. Age model

We adapted an age modeling routine which estimates seasonally changing growth rates and the timing of shell formation in bivalves from  $\delta^{18}\text{O}_\text{c}$  profiles by Judd et al. (2018) in Matlab (Mathworks, Nantick, MA, USA; script given in [Supplementary Information](#)) to work with high-resolution  $\mu\text{XRF}$  Mg/Ca data (see 2.4). Mg/Ca profiles were smoothed using a moving average and normalized before applying the modeling routine (following Durham et al., 2017). To prevent bias on Mg concentrations introduced by microstructural change, age models were based solely on Mg/Ca profiles that were measured entirely in



the foliated microstructure. A date relative to the annual cycle was assigned to each  $\mu$ XRF measurement point by combining growth rate and temperature sinusoids to simulate the Mg/Ca curve until an optimal fit with the data was achieved (see Judd et al., 2018). This relative age model was anchored to real calendar dates by linking the most recently deposited shell material to the date of shell harvest. The age model was then projected on  $\mu$ XRF lines through both microstructures using the position of the line scans and the position of both lines on the same shell were correlated visually based on microscopic growth increments observable on color scans (see Fig. 4). Relative timing of both  $\mu$ XRF profiles was validated by comparing their Sr/Ca profiles. Ages of shell portions were converted to calendar dates by anchoring the youngest portions of the shell to the harvest date of the specimen. Results of age modeling are provided in the **Supplementary Information**. The age model allowed the presence of microstructures to be assessed relative to the time of year, and a sinusoidal regression was used to test for seasonality in the expression of microstructures in the shells (see **Supplementary Information**).

## 2.6. Ambient sea water conditions

High-resolution (hourly) time series of temperature and salinity were measured *in situ* on the jetty of the Netherlands Institute for Sea Research (NIOZ) located on the southern coast of the island of Texel (53°0.1' N latitude and 4°47.3' W longitude) within 5 kilometers from the sample location for the Mokbaai and TESO harbor samples (M1-6 and H1-4; see Fig. 1). Data from the NIOZ jetty for the period from 2001 up to and including 2018 was collected by an Aanderaa 3210 ST sensor using a type 3634 Datalogger (prior to May 2016), an Aanderaa IW3919 (May 2016 – August 2017) and an EXO2 Sonde with wiped Conductivity and Temperature sensor (YSI inc., September 2017–present). Observations were taken every 10 seconds at a depth of –1.5 N.A.P. Data was calibrated with separate T (using Handheld Testo Thermometer) and S measurement (using a Guild Autosol salinometer) taken every week,

and median hourly values were derived (**Supplementary Information**). This location experienced a seasonal temperature range of 3–21 °C (based on daily averages, the monthly average temperature range is 3–19 °C; see **Supplementary Information**) with a mean annual average of 11 °C and daily salinity range of 25–32 (based on daily averages, the monthly average SSS range is 26.6–29.1; see **Supplementary Information**) around an annual mean of 28. With a local water depth of 3.0 m the site of the NIOZ jetty is generally well mixed, so that temperature and salinity can be assumed to reflect sea surface temperature (SST) and sea surface salinity (SSS) SST and SSS time series for Brittany were obtained from a compilation of *in situ* SST and SSS measurements from local stations, data from which were obtained from the Institut Français de Recherche pour l'Exploitation de la Mer (IFREMER, Issy-les-Moulineaux, France; <http://www.ifremer.fr/co-en/>, last access 18/05/2020 see **Supplementary Information**). The Brittany locality experienced a seasonal SST range of 5–21 °C with a mean annual average of 13.6 °C and an SSS range of 32–35 around an annual mean of 33. In absence of *in situ* sea water  $\delta^{18}\text{O}_w$  concentrations, sea water elemental and  $\delta^{18}\text{O}$  composition was calculated assuming mixing of mean ocean water ( $\delta^{18}\text{O}_w \equiv 0 \text{‰ VSMOW}$ ) with freshwater with a  $\delta^{18}\text{O}_w$  of  $-7.9 \text{‰ VSMOW}$  (Mook, 1970; IAEA, 2015; Bowen, 2020; details in **Supplementary Information**). Note that seasonal variations in Mn concentration of the water may be affected by local processes such as varying terrestrial input and oxygenation which are not controlled in this study (van Hulst et al., 2016). Sub-annual age models (see 2.5) were used to calculate elemental (Na, Mg, S, Cl, Ca, Mn and Sr) concentrations and water temperatures weighed against growth rate seasonality for both microstructures for comparison with shell chemistry results.

## 2.7. Calculation of empirical element distribution coefficients

Empirical distribution coefficients (D) for the elements Na, Mg, Cl, S, Mn and Sr between calcite of the foliated and chalky microstructures and seawater were calculated from concentrations in these microstructures and concen-



Fig. 3. Compilation of microscopic images of the two microstructures in the hinge region of *C. gigas*. In all images, “f” denotes occurrence of the foliated microstructure while “c” indicates where the chalky structure is exposed. **A**) Composite of reflected light microscopy images of the hinge region of sample O2 before Mutvei staining (opposite side of the cross-section shown in Fig. 2). **B**) Composite of reflected light microscopy images of the hinge region of sample O2 after Mutvei staining, with “DZ” and “LZ” indicating the occurrence of dark and light bands in the foliated microstructure (sensu Higuera-Ruiz and Elorza, 2009) **C**) SEM close-up image of a region where the edge of a lens of chalky structure is visible between foliated calcite layers. **D**) SEM close-up of the tip of a lens of chalky structure, which tapers off in between foliated laminae. Note how foliated laths on the right side (dorsal side, deposited before the chalky structure) of the lens change orientation towards the chalky structure and transition into the chalky microstructure. **E**) SEM close-up of chalky microstructure showing the irregular orientation of calcite blades and the large, interconnected pore space in between. **F**) SEM close-up of the foliated microstructure showing densely packed calcite folia with changes in mineral orientation, which become more common close to the outer margin of the hinge (bottom of **A** and **B**). **G**) SEM close-up of the transition from foliated (right, or dorsal side, deposited first) to chalky (left, or ventral side, deposited afterwards) calcite showing how the foliated calcite laths smoothly transition into the chalky microstructure by changing their orientation and loosening their packing. **H**) SEM close-up of chalky microstructure (right, dorsal side) transitioning into foliated microstructure (left, ventral side, deposited after chalky microstructure). Note how the oldest foliated laths on the bottom of the image (in direction of the hinge) taper out into the chalky structure while folia deposited afterwards (farther to the left, or ventral, side) continue further. Note also that the folia are initially less densely packed, organized in bundles, and regain their typical structure later (compared with **D** and **F**). Full size SEM images are provided in **Supplementary Information**. Arrow labeled “d.o.g.” indicates direction of growth.

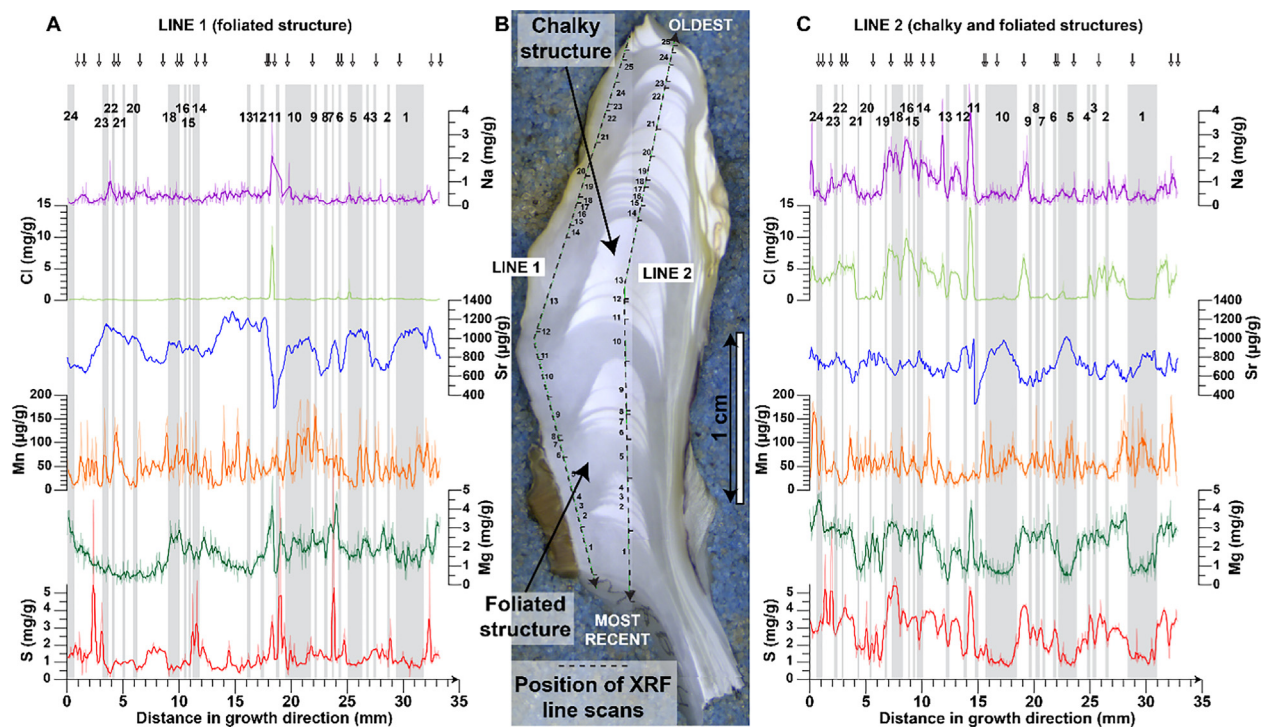


Fig. 4. Examples of high-resolution X-Ray Fluorescence profiles through the hinge of specimen **M5**. Profiles are plotted in direction of growth from the outer (top in image **B**) to the inner surface (bottom in image **B**) of the shell, or: from oldest to most recently formed shell material (see dashed arrows in **B**). Plots **A** and **C** show concentrations of (from top to bottom) Na (purple), Cl (light green), Sr (dark blue), Mn (orange), Mg (dark green) and S (red) in profiles exclusively through the foliated structure (line 1; **A**) and through both structures (line 2, **B**) respectively. Arrows above these plots indicate the locations of tick marks on the dashed arrows in **B**, while numbers below the arrows count the number of foliated layers in line 2 (**C**) and their contemporary locations in line 1 (**A**). The locations of these foliated layers were used to temporally align parts of the profiles that represent shell material that formed simultaneously.

trations of the respective elements in seawater at the time of shell formation using the following equation:

$$D_X = \frac{[X]_{\text{carbonate}}/[Ca]_{\text{carbonate}}}{[X]_{\text{seawater}}/[Ca]_{\text{seawater}}}$$

Here,  $X$  represents an element and  $D_X$  is the distribution coefficient of that element between water and shell biomineral carbonate of the respective microstructure. Detailed documentation of the position of these  $\mu$ XRF profiles allowed each data point to be placed either within the foliated or chalky microstructure (see Fig. 4). As a result, seasonally weighted averaged distribution coefficients for both microstructures could be calculated for specimens **O1-8**, **M4-6** and **H4** by averaging the distribution coefficients calculated individually for each data point within microstructures. Uncertainties on distribution coefficients were calculated as 95 % confidence levels based on variability within microstructures in each specimen. These uncertainties include uncertainties on dating and alignment of the microstructures using the age model. Elemental distribution coefficients for both microstructures in all specimens are provided in [Supplementary Information](#). Response of distribution coefficients, microstructure expression, and growth rate to seasonal variability in the environment was investigated using sinusoidal regression (see [Supplementary Information](#)). We aggregate the results of significance tests on

individual specimens for each variable using Fisher's method (Fisher, 1932) to test whether the variable has a seasonal component.

## 2.8. Carbon and oxygen isotopic analysis

Small (20–45  $\mu$ g) aliquots of calcite were drilled from the hinges of specimens **H1**, **M1** and **M2** in the direction of the axis of maximum growth using a high-precision, computer-driven Micromill (ESI, Portland, OR, USA) attached to an x, y and z stage following digitized milling path positions. Calcite carbon ( $\delta^{13}\text{C}_c$ ) and oxygen ( $\delta^{18}\text{O}_c$ ) isotope values were measured using an automated carbonate device (Thermo-Kiel 105 IV) connected to a Thermo Finnigan MAT 253 Dual Inlet Isotope Ratio Mass Spectrometer (IRMS) at the Royal Netherlands Institute for Sea Research (NIOZ). NBS-19 limestone was used as standard material for the calibration, while the Vrije Universiteit Internal Carbonate Standard (VICS:  $\delta^{18}\text{O}_c = -5.44\text{‰}$ ;  $\delta^{13}\text{C}_c = 1.35\text{‰}$ ; [Pracht et al., 2018](#)) was measured after every seventh sample and used for drift detection and correction. External precision, measured as 95 % confidence level based on variability within NBS-19 standard measurements, was always better than 0.1‰ for both  $\delta^{18}\text{O}_c$  and  $\delta^{13}\text{C}_c$ . All stable isotope ratio results are provided in [Supplementary Information](#).



## 2.9. Carbonate clumped isotope analysis

Larger calcite samples (~15 mg) were drilled from both the foliated and chalky microstructure of specimens **M2** and **M6** for clumped isotope analyses using a handheld Dremel 3000 (Robert Bosch GmbH, Racine, WI, USA) rotary drill equipped with a tungsten carbide drill bit ( $\varnothing = 1$  mm). An excess amount of sampling of both microstructures was done along multiple growth years in the hinge of the specimens to ensure proper mixing of the seasonal variability recorded in the shell. Multiple ~90  $\mu\text{g}$  aliquots from homogenized samples of the foliated (23 aliquots) and chalky (23 aliquots) structure of **M2** and the foliated (18 aliquots) and chalky (19 aliquots) of **M6** were analyzed using a Thermo Fisher Scientific MAT253 PLUS mass spectrometer coupled to a Kiel IV carbonate preparation device. Aliquots were reacted at 70 °C with nominally anhydrous (103 %) phosphoric acid. The resulting  $\text{CO}_2$  gas was cleaned from water and organic compounds with two cryogenic liquid  $\text{N}_2$  traps and a PoraPak Q trap kept at -40 °C. The purified sample gases were analyzed in micro-volume LIDI mode with 400 s integration time against a clean  $\text{CO}_2$  working gas ( $\delta^{13}\text{C}_c = -2.82$  ‰VPDB;  $\delta^{18}\text{O}_c = -4.67$  ‰VPDB), corrected for the pressure baseline (Bernasconi et al., 2013; Meckler et al., 2014) and converted into the absolute reference frame by computing an empirical transfer function from ETH calcite standards (ETH-1, -2, -3) analyzed on different days and their accepted values (Bernasconi et al., 2018; Kocken et al., 2019). Sample data were corrected for drift by bracketing with ETH-3 standard aliquots. All isotope ratio data were calculated using IUPAC parameters following Daëron et al. (2016) and  $\Delta_{47}$  values were projected to a 25 °C acid reaction temperature with a correction factor of 0.062‰ (after Defliese et al., 2015; Murray et al., 2016). Long-term  $\Delta_{47}$  reproducibility standard deviation was determined to be 0.04‰ based on repeated measurements of ~90  $\mu\text{g}$  aliquots of our control standard IAEA C2 ( $\Delta_{47}$  of 0.719‰; measured over a 20-month period; see [Supplementary Information](#)). Calcification temperatures were calculated from  $\Delta_{47}$  values using the temperature calibration by Kele et al. (2015) modified by Bernasconi et al. (2018). For the  $\delta^{18}\text{O}_c$  values, we applied an acid correction factor of 1.00871 (Kim and O'Neil, 1997). Both  $\delta^{18}\text{O}_c$  and  $\delta^{13}\text{C}_c$  were reported versus VPDB with a typical reproducibility below 0.08‰ and 0.04‰, respectively (95 % confidence level). To calculate the  $\delta^{18}\text{O}_w$  from  $\Delta_{47}$  and  $\delta^{18}\text{O}_c$ , we used the  $\delta^{18}\text{O}_c$ -temperature relationship of Kim and O'Neil (1997). Only  $\delta^{18}\text{O}_c$  values from aliquots used for  $\Delta_{47}$  measurements were used to calculate  $\delta^{18}\text{O}_w$ . The number of  $\Delta_{47}$  aliquots per sample enabled temperature estimates from  $\Delta_{47}$  in foliated and chalky microstructures with an uncertainty of  $\pm 3.3$  °C (95 % confidence level). Raw data and metadata associated with all clumped isotope analyses are provided in [Supplementary Information](#).

## 2.10. Nitrogen isotopic analysis

We determined nitrogen isotope ratios ( $\delta^{15}\text{N}$ ) of organic matter bound to calcite in the foliated and chalky

microstructures of specimens **M2**, **M6**, **H2** and **H3** on the same samples used for carbonate clumped isotope analyses (see details in [Supplementary Information](#)). Briefly, calcite samples were subjected to reductive and oxidative cleaning. After cleaning, samples were dissolved in acid, and calcite-bound organic N was oxidized to nitrate using a basic solution of potassium peroxydisulfate ( $\text{K}_2\text{S}_2\text{O}_8$ ) following the protocols previously described for other fossil types (e.g. foraminifera, corals, bioapatite and otoliths; Ren et al., 2009; Straub et al., 2013; Wang et al., 2014; 2016; Lueders-Dumont, 2018; Leichter et al., 2021). The isotopic composition and N content were measured using the 'denitrifier method', in which nitrate is quantitatively converted to nitrous oxide ( $\text{N}_2\text{O}$ ) by denitrifying bacteria (Sigman et al., 2001; Weigand et al., 2016). The external precision of our  $\delta^{15}\text{N}$  results, calculated at the 95% confidence level of repeated analyses on in-house coral standards across multiple batches analyzed was 0.20‰.

## 2.11. Sulfur isotopic analysis

The isotopic composition ( $\delta^{34}\text{S}$ ) of carbonate-associated sulfur in the foliated and chalky structure of specimens **H2** and **H3** was measured using a multi-collector - inductively coupled plasma - mass spectrometer (MC-ICP-MS; Neptune XT, Thermo Fisher Scientific, Bremen, Germany). Our instrumental setup and sample preparation were based on methodology detailed in Paris et al. (2013). Details on sample preparation, instrumental setup and data treatment are reported in [Supplementary Information](#). Due to the large (100–160 mg) sample size required for the  $\delta^{34}\text{S}$  analyses, the number of full replicates per microstructure within shells was limited and multiple digestions for each sample were not possible to estimate the uncertainty of the whole procedure. The expanded uncertainty (95 % confidence level) of  $\delta^{34}\text{S}$  measurements on individual samples was determined to be 0.55‰ based on standard deviation from two carbonate non-isotopic certified reference materials (BAS ECRM782-1 dolomite; Bureau of Analysed Samples Ltd., Middlesbrough, UK and NIST-1d limestone; National Institute of Standards and Technology, Gaithersburg, MD, USA) which have been taken through the whole sample preparation procedure during at least 5 separate occasions and measured in total at least 29 times on different days. Uncertainties on mean  $\delta^{34}\text{S}$  per microstructure were calculated by combining individual  $\delta^{34}\text{S}$  measurement uncertainties into one 95 % confidence level per microstructure (see [Table 3](#) and [Supplementary Information](#)).

## 3. RESULTS

### 3.1. Microscopy

Composite reflected light microscopy images ([Fig. 3A-B](#); [Supplementary Information](#)) show that lenses of chalky microstructure are intercalated between layers of foliated calcite. Under visible light, the chalky microstructure appears opaque and milky white, while the foliated

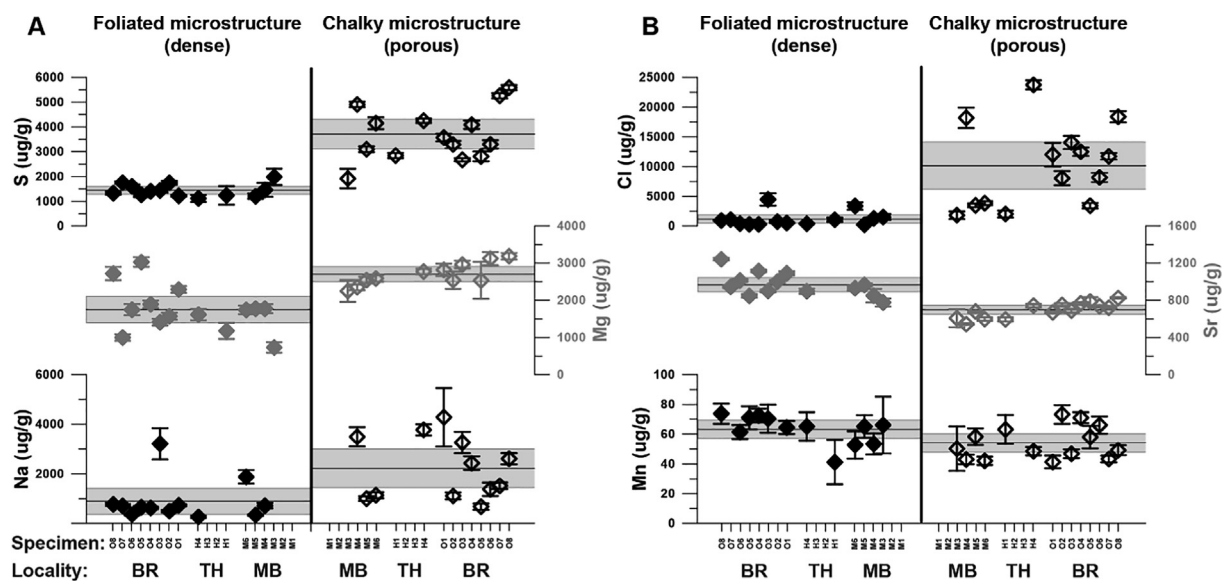


Fig. 5. Overview of average concentrations of A) Na (black), Mg (grey) and S (black) and B) Cl (black), Sr (grey) and Mn (black) in the foliated (closed symbols, left) and chalky (open symbols, right) microstructures. Specimens are grouped by locality: BR = Brittany (specimens O1-8), TH = TESO Harbor (Specimens H1-4) and MB = Mokbaai (Specimens M1-6). Error bars on symbols represent 95 % confidence level estimates on concentrations within specimens. Wide shaded error bars spanning all specimens indicate 95 % confidence levels of inter-specimen variability for the same microstructure.

structure is translucent grey. Under higher magnification using SEM, it becomes clear that these differences stem from the microscopic organization of both microstructures: Chalky structures are composed of loosely organized blades of calcite with ample interconnected porosity (Fig. 3E and G), while the foliated structure consists of densely packed calcite laths organized in semi-parallel bands (Fig. 3D, F and H), as observed by Carriker et al. (1980). The proportions of chalky and foliated microstructure differ strongly between specimens (Fig. 2). There is no clear consistency in the occurrence microstructures in shells of specimens grown in the same environment or in the same growth years (see Fig. 2). Mutvei staining (Fig. 3B) also allows variations within the foliated microstructure to become visible, highlighting a distinct pattern of dark and light zones (“DZ” and “LZ” respectively) as described for *C. gigas* by Higuera-Ruiz and Elorza (2009).

SEM close-ups show that at boundaries on the dorsal (right in Fig. 3) side of lenses of chalky structure, where chalky microstructure is precipitated on top of foliated layers, foliated laths change their orientation towards the chalky structure when approaching the boundary, breaking the rigidly organized foliated structure (Fig. 3D and G). On the other side of lenses, where foliated structures are deposited on top of chalky structures, bundles of calcite laths are deposited at a slight angle with respect to the boundary, with some bundles overlapping on (tapering out against) the microstructural boundary (Fig. 3D and H). Finally, bundles of laths in the foliated structure deposited directly on top of chalky structure are more widely spaced, after which the consecutive bundles gradually regain their typical dense packing (Fig. 3H).

### 3.2. Elemental concentrations

XRF analysis yielded high-resolution profiles through foliated and chalky microstructures and allowed differences in elemental (Na, Mg, S, Cl, Mn and Sr) composition between the microstructures to be studied in detail (see Fig. 4 for an example and [Supplementary Information](#) for raw data). Correlation between XRF profiles using color scans and microscopy allowed chalky and foliated calcite that mineralized at the same time to be directly compared. This comparison eliminates environmental or ontogenetic effects and allows the effect of the microstructure type on shell composition to be studied in isolation. Variability of different XRF measurements within the same microstructure are used to quantify uncertainty to include both variability within the shell and measurement uncertainty while comparing between microstructures. There is a significant ( $p < 0.05$ ; Student t-test) difference in the concentrations of all trace elements between microstructures (Fig. 5 and Table 1). Concentrations of Na, Mg, S and Cl in chalky microstructures more closely resemble those of ambient seawater (Pilson, 2012; van Hulst et al., 2016) than those of the foliated microstructure ([Supplementary Information](#)).

### 3.3. Age model

Periodic variation in Mg concentrations is observed in those XRF profiles which exclusively sample the foliated structure, while these variations are obscured by the alternations between chalky and foliated microstructures in the profiles crossing both microstructures (Fig. 4). Variability in Mg concentrations through the foliated calcite is

Table 1

Summary of elemental concentrations in the foliated and chalky microstructure of *C. gigas* as measured by  $\mu$ XRF. Uncertainties are reported as 95 % confidence levels and rounded to nearest significant figures (raw data reported in **Supplementary Information**).

Locality	Micro-structure	Na ( $\mu$ g/g)		Mg ( $\mu$ g/g)		S ( $\mu$ g/g)		Cl ( $\mu$ g/g)	
TH & MB	Chalky	2300	$\pm 1700$	2500	$\pm 1000$	3530	$\pm 1100$	8900	$\pm 9600$
	Foliated	800	$\pm 710$	1470	$\pm 430$	1400	$\pm 650$	1300	$\pm 1100$
BR	Chalky	2150	$\pm 990$	2900	$\pm 1100$	3810	$\pm 880$	10,900	$\pm 3700$
	Foliated	940	$\pm 760$	1960	$\pm 560$	1470	$\pm 170$	1100	$\pm 1100$
Combined	Chalky	2220	$\pm 780$	2690	$\pm 200$	3690	$\pm 610$	10,000	$\pm 3900$
	Foliated	900	$\pm 530$	1750	$\pm 350$	1440	$\pm 160$	1180	$\pm 720$

Locality	Micro-structure	Mn ( $\mu$ g/g)		Sr ( $\mu$ g/g)		Ca (wt %)	
TH & MB	Chalky	51	$\pm 8$	628	$\pm 71$	38.0	0.8
	Foliated	57	$\pm 10$	880	$\pm 370$	38.5	1.1
BR	Chalky	56	$\pm 10$	737	$\pm 41$	38.0	0.4
	Foliated	69	$\pm 26$	1020	$\pm 100$	39.1	0.1
Combined	Chalky	54	$\pm 6$	690	$\pm 46$	38.0	0.3
	Foliated	63	$\pm 6$	966	$\pm 76$	38.8	0.4

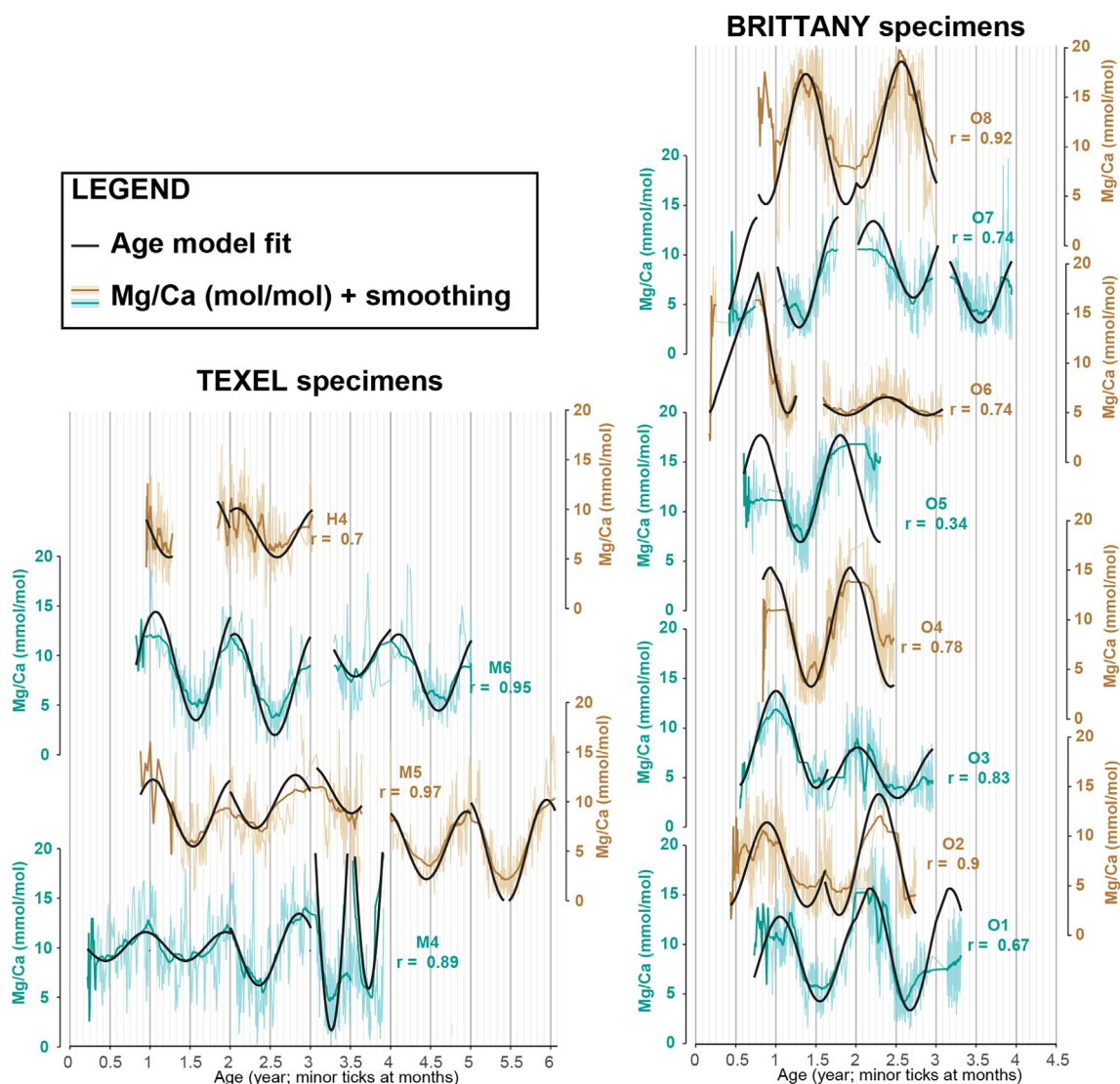


Fig. 6. Overview of Mg/Ca profiles through foliated calcite in all specimens (light brown and blue lines), smoothed Mg/Ca profiles (Dark brown and blue lines; see **Supplementary Information**) and approximations of the Mg/Ca profiles by the age model routine (thick black lines) plotted against modelled shell age. Axes are equally scaled for all specimens. Alternating colors of specimens are only used to promote distinction between records. Major vertical grid lines indicate half-year marks and minor gridlines are monthly spaced. R-values represent Pearson  $r$  correlations between Mg/Ca records and their approximations by the age model.

therefore independent of the pattern of microstructural change in the shell hinge. Application of the modified age model on Mg/Ca records reveals that a combination of sinusoids for growth rate and seasonality can be used to accurately describe this variability in Mg/Ca ratios (Mean Pearson  $r$  value = 0.79; see Fig. 6). Specimens with the shortest Mg/Ca records (e.g. O5) tend to have the lowest correlation between measured Mg/Ca and model fit. The occurrence of multiple growth stops, especially near the beginning or end of the Mg/Ca record (e.g. O6 and O7) as well as the presence of strong sub-annual Mg/Ca variability (e.g. specimen H4 and O1) also reduces the model fit. Regardless of these complications, seasonal scale variability in Mg/Ca in *C. gigas* profiles is closely approximated by the model (Fig. 6). More details on age modeling results, including plots of Mg/Ca records and their approximations against depth and time, are provided in Supplementary Information

Growth stops do occur in *C. gigas* in all localities, these are generally short-lived (with some exceptions in H4, M4 and O7), and are not concentrated in a specific season

(Fig. 6). Final ages of individuals vary between 1.6 (specimen O4) and 5.2 years (specimen M5) with an average of 3.0 years, with the larger specimens from Texel (TH and MB) being on average older ( $4.2 \pm 2.1$  years) than Brittany specimens (BR;  $2.5 \pm 0.7$  years; 95 % CL; Fig. 6 and Supplementary Information). Growth rate along the axis of maximum growth is significantly higher in the chalky microstructure ( $42.7 \pm 5.4$   $\mu\text{m}/\text{d}$ ) than in the foliated microstructure ( $33.0 \pm 4.2$   $\mu\text{m}/\text{d}$ ; Supplementary Information).

### 3.4. Empirical distribution coefficients

Empirical distribution coefficients ( $D$ ) of trace elements were calculated from temporally aligned XRF records of element concentrations (see 2.7; Fig. 7; Table 2; see Supplementary Information). These estimates are independent of seasonal variability in growth rate and SSS, as opposed to estimates of the  $D$  from average concentrations of seawater, chalky and foliated calcite, which may be biased if microstructures are over-represented in a specific season

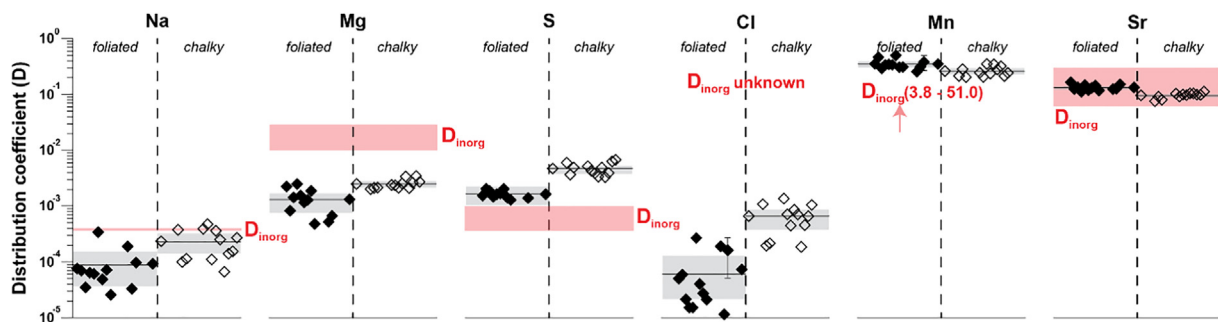


Fig. 7. Distribution coefficients ( $D_{\text{oyster}}$ ) of Na, Mg, S, Cl, Mn and Sr for the chalky (open symbols) and foliated (closed symbols) microstructures in *C. gigas*. Wherever error bars are not shown for estimates for individual specimens, the uncertainty (95 % confidence level) is within the size of the symbol. Shaded grey bars indicate variability within microstructures, with solid lines indicating the average value for the microstructure. Red bars and numbers indicate literature values for  $D_{\text{inorg}}$  (Kitano et al., 1975; Rimstidt et al., 1998; Day and Henderson, 2013; van Dijk et al., 2017; Hauzer et al., 2018). Note the logarithmic scale on the vertical axis.

Table 2

Overview of distribution coefficients ( $D$ ) of Na, Mg, S, Cl, Mn and Sr between foliated and chalky microstructures and seawater as well as the average SST and SSS under which these microstructures are formed. Note that values for  $D_{\text{Na}}$ ,  $D_{\text{Mg}}$ ,  $D_{\text{S}}$ ,  $D_{\text{Cl}}$  and  $D_{\text{Sr}}$  are multiplied by a factor (behind brackets in column header) for clarity. Uncertainties are given as 95 % confidence levels.

Locality	Microstructure	$D_{\text{Na}} (*10^5)$	$D_{\text{Mg}} (*10^4)$	$D_{\text{S}} (*10^4)$	$D_{\text{Cl}} (*10^5)$
TH & MB	Chalky	25 $\pm$ 12	21.7 $\pm$ 1.3	49.5 $\pm$ 7.0	71 $\pm$ 42
	Foliated	8.6 $\pm$ 5.6	5.6 $\pm$ 1.3	13.5 $\pm$ 2.1	9.6 $\pm$ 8.7
BR	Chalky	22.8 $\pm$ 6.9	26.6 $\pm$ 2.5	46.0 $\pm$ 4.2	63 $\pm$ 10
	Foliated	9.6 $\pm$ 4.0	16.1 $\pm$ 1.9	17.1 $\pm$ 1.1	6.2 $\pm$ 3.6
COMBINED	Chalky	23.4 $\pm$ 5.5	25.0 $\pm$ 1.9	47.2 $\pm$ 2.8	66.1 $\pm$ 9.8
	Foliated	9.3 $\pm$ 3.0	13.2 $\pm$ 1.6	16.4 $\pm$ 1.1	7.3 $\pm$ 4.3
Locality	Microstructure	$D_{\text{Mn}}$	$D_{\text{Sr}} (*10^3)$	SST	SSS
TH & MB	Chalky	0.2 $\pm$ 0.0	87.9 $\pm$ 9.0	12.1 $\pm$ 1.5	28.0 $\pm$ 0.3
	Foliated	0.3 $\pm$ 0.1	131 $\pm$ 11	12.2 $\pm$ 2.0	28.1 $\pm$ 0.3
BR	Chalky	0.3 $\pm$ 0.0	101.0 $\pm$ 3.2	12.4 $\pm$ 0.6	33.6 $\pm$ 0.2
	Foliated	0.4 $\pm$ 0.0	135.2 $\pm$ 5.3	12.0 $\pm$ 0.5	33.5 $\pm$ 0.1
COMBINED	Chalky	0.3 $\pm$ 0.0	96.6 $\pm$ 3.1	12.3 $\pm$ 0.6	31.7 $\pm$ 0.5
	Foliated	0.4 $\pm$ 0.1	133.8 $\pm$ 4.3	12.1 $\pm$ 0.6	31.7 $\pm$ 0.5

Table 3

Overview of stable isotope ratio data of *C. gigas* microstructures. Reconstructed sea surface temperatures were calculated from  $\Delta_{47}$  values and  $\delta^{18}\text{O}_w$  values were calculated from a combination of SST and  $\delta^{18}\text{O}_c$ . Uncertainties are given as 95 % confidence level.

Microstructure	$\delta^{34}\text{S}$ (‰VCDT)		$\delta^{15}\text{N}$ (‰AIR)		$\delta^{18}\text{O}_c$ (‰VPDB)		$\delta^{13}\text{C}_c$ (‰VPDB)	
Chalky	20.9	±0.4	13.5	±0.3	−1.67	±0.12	−1.91	±0.09
Foliated	20.4	±0.4	13.9	±1.7	−1.39	±0.13	−1.87	±0.05
Microstructure	$\Delta_{47}$ (‰)		SST (°C)		$\delta^{18}\text{O}_w$ (‰VSMOW)			
Chalky	0.706	±0.012	15.3	±3.3	−1.83	±0.73		
Foliated	0.689	±0.012	20.0	±3.3	−0.77	±0.72		

or develop preferably under specific conditions. Empirical distribution coefficients of Na, Mg, S and Cl are significantly higher for the chalky microstructure compared to the foliated microstructure and distribution coefficients for Mn and Sr are significantly lower ( $p < 0.05$ ; Student t-test). Comparison of the estimated D values of Na, Mg, S, Mn and Sr ( $D_{\text{oyster}}$ ) with D values of inorganic calcite ( $D_{\text{inorg}}$ ) from the literature (Kitano et al., 1975; Rimstidt et al., 1998; Day and Henderson, 2013; van Dijk et al., 2017; Hauzer et al., 2018) shows that  $D_{\text{oyster}}$  of Mg and Mn are significantly lower than  $D_{\text{inorg}}$  ( $p < 0.05$ ; z-test),  $D_{\text{oyster}}$  of Na and S are higher than  $D_{\text{inorg}}$ , and  $D_{\text{oyster}}$  of Sr is not statistically different from  $D_{\text{inorg}}$ . No  $D_{\text{inorg}}$  data for Cl were available.

### 3.5. Seasonality in microstructures and distribution coefficients

Sinusoidal regressions (see [Supplementary Information](#)) only showed significant annual periodicity in the prevalence of microstructures in 2 out of 12 shells (specimens **M4** and **O1**; see [Supplementary Information](#)). When combining tests from individuals using Fisher's  $\chi^2$ -test, the global seasonal expression of microstructures is not significant ( $p = 0.08$ ) based on the trace element profile that crosses multiple microstructures. If present, this periodicity (seasonality) explains roughly half of the variability (adjusted  $R^2 \approx 0.50$ ; [Supplementary Information](#)). Empirical trace element distribution coefficients only exhibit a seasonal component in, on average, 3–4 of the 12 specimens with little coherence between specimens. Combined tests do yield significant seasonal variability in distribution coefficients (Fisher's  $\chi^2$ -test  $p < 0.05$ ), but on an individual level there is no consistent seasonal relationship with trace element distribution coefficient. Wherever the relationship passes significance testing the relationship with seasonal variability is weak ( $R^2 < 0.60$ ) and inconsistent between Texel and Brittany. The empirical distribution coefficient of Mg is most seasonal, with a statistically significant seasonal component in 6 out of 12 specimens and with strong correlation ( $R^2 = 0.75$  on average; Fisher's  $\chi^2$ -test  $p \ll 0.01$ ). This strong correlation is striking considering the high degree of sub-annual variability and the variability in linear growth rate observed in Mg/Ca profiles, which explains why some specimens (e.g. specimen **H4**; see [Fig. 6](#)) fail to show a significant correlation with a sinusoidal fit. There is no consistency in the phase of seasonal components in distribution coefficients. Linear growth rate in sampling

direction shows a strong (adjusted  $R^2 \approx 0.80$ ) significant seasonal component in all but one specimen (specimen **O5**;  $p = 0.07$ ; Fisher's  $\chi^2$ -test  $p \ll 0.01$ ).

### 3.6. Stable isotope values

An overview of stable isotope values determined in both microstructures is given in [Fig. 8](#) and [Table 3](#). On average, the two microstructures of *C. gigas* are highly isotopically similar. The only statistically significant ( $p < 0.05$ ; Student t-test) difference between chalky and foliated calcite is observed for  $\delta^{18}\text{O}_c$  and  $\Delta_{47}$  values. In addition,  $\delta^{18}\text{O}_c$ ,  $\delta^{13}\text{C}_c$  and  $\delta^{15}\text{N}$  values exhibit significant inter-specimen variability. Large variability in  $\delta^{18}\text{O}_c$  and  $\delta^{13}\text{C}_c$  between and within some specimens is mostly observed in specimens **H1**, **M1** and **M2**, which were microsampled and therefore include seasonal variability (see [2.5](#) and [Supplementary Information](#)), while bulk sampled specimens **M2** and **M6** for combined  $\Delta_{47}$ ,  $\delta^{18}\text{O}_c$  and  $\delta^{13}\text{C}_c$  analyses show less internal variability (see [Fig. 7](#)). Temperatures reconstructed from separate  $\Delta_{47}$  measurements on chalky and foliated microstructure significantly ( $p < 0.05$ ; z-test; see [Figs. 8](#) and [S11](#)) overestimate the actual mean annual SST by 3.8 °C (+3.3 / −3.2 °C; 95 % confidence level) and 8.5 °C (+3.4 / −3.3 °C; 95 % confidence level), respectively but fall within the seasonal SST range experienced by the specimens (3–21 °C; see [2.6](#) and [Supplementary Information](#)). The spread in  $\Delta_{47}$  is large enough to assume the results from foliated and chalky microstructure to be sampled from different distributions with statistically different means (Kolmogorov-Smirnov Test:  $p = 0.03$ ; Student t-test  $p = 0.04$ ; [Supplementary Information](#)). Combining all measurements from both microstructures yields an average temperature of 17.6 (+2.4 / −2.3 °C; 95 % confidence level), which is 6.1 °C warmer than mean annual temperature ( $p < 0.05$ ; z-test). Reconstructed  $\delta^{18}\text{O}_w$  data are not statistically different from those calculated from *in situ* SSS measurements in the environment ( $-1.31 \pm 0.51\text{‰VSMOW}$ ; 95 % confidence level) and fall within the typical  $\delta^{18}\text{O}_w$  range reported in previous studies on the Wadden Sea (between −0.8 and −3.3‰VSMOW for a typical SSS range of 27–33 psu; Witbaard et al., 1994; Böttcher et al., 1998; Harwood et al., 2008). However, foliated calcite yields slightly higher values than the mean annual  $\delta^{18}\text{O}_w$  ( $-0.77 \pm 0.71\text{‰VSMOW}$ ; equivalent to summer values) and chalky structures yield slightly lower  $\delta^{18}\text{O}_w$  values ( $-1.83 \pm 0.73\text{‰VSMOW}$ ; closer to winter values; [Fig. 8](#); [Supplementary Information](#)). The foliated calcite exhibited statisti-

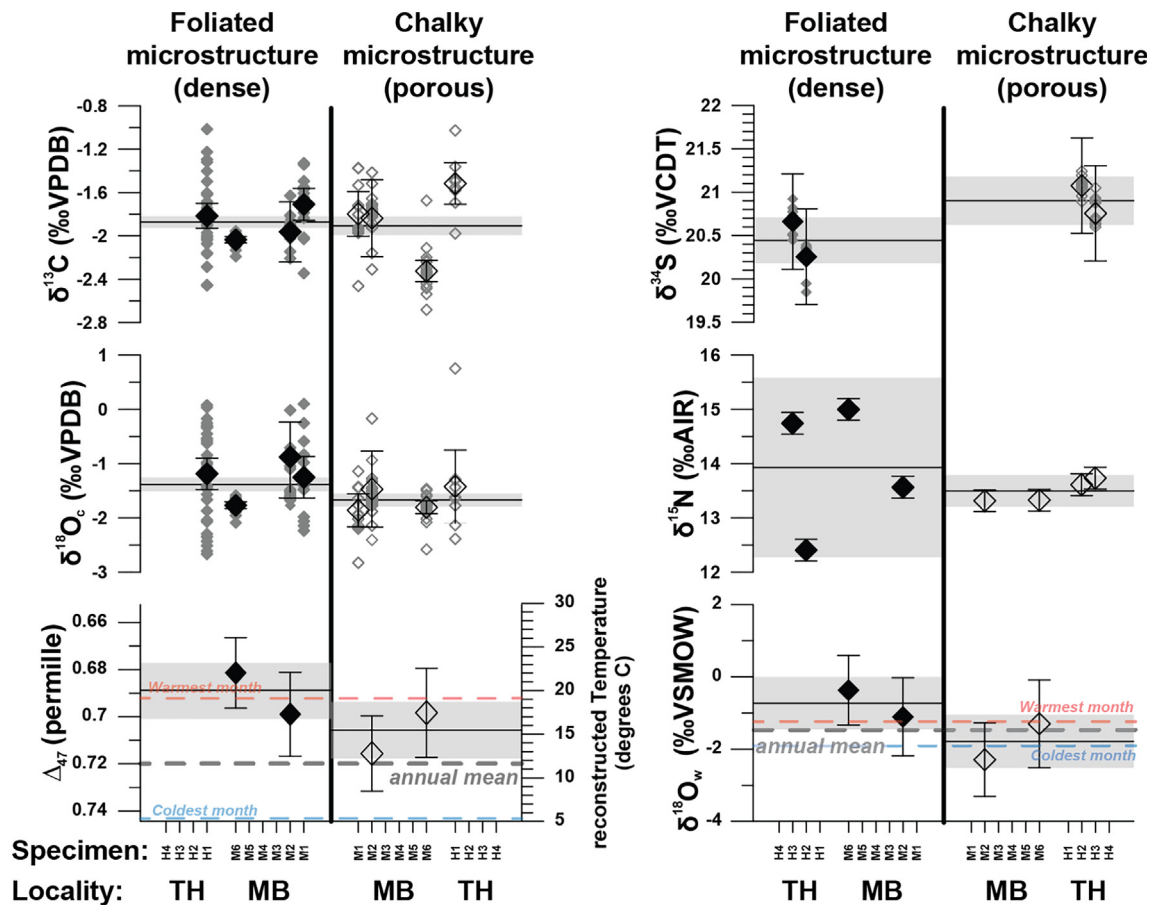


Fig. 8. Overview of stable isotope ratio data of foliated (left, closed symbols) and chaly (right, open symbols) microstructures in *C. gigas*. Color coding of symbols and error bars follows that in Fig. 5. Horizontal black, red and blue dashed lines indicate annual mean, summer month and winter month SST and SSS derived from in situ measurements at the NIOZ jetty.

cally significant inter-specimen differences in  $\delta^{15}\text{N}$ , which are not observed in chaly microstructures. Inter-specimen differences in  $\delta^{15}\text{N}$  of the foliated microstructure are substantial (inter-specimen standard deviation = 1.19 ‰) compared to those in the chaly microstructure (SD = 0.21 ‰) and exceed analytical uncertainty (SD of 0.20 ‰, see 2.10 and Supplementary Information). Variability in  $\delta^{34}\text{S}$  between specimens and microstructures is small (<1 ‰VCTD) and generally smaller than variability within specimens. It can be fully attributed to analytical uncertainty since different aliquots of the same homogenized sample were measured for each specimen and microstructure. As a result, it can be concluded that there is no significant inter-specimen isotopic variability.

## 4. DISCUSSION

### 4.1. Timing of growth in *C. gigas*

#### 4.1.1. Mg/Ca seasonality

Microgrowth increments are often used to assess the timing and growth rate of bivalve shell carbonate (e.g. Jones, 1983; Schöne et al., 2005b). However, some bivalve species mineralize shells without clearly identifiable micro-

growth patterns (such as those of *C. gigas*; Huyghe et al., 2019). In these cases, alternative techniques are developed to estimate seasonally varying growth rates and reconstruct the timing of shell growth based on the strong relationship between  $\delta^{18}\text{O}_c$  and temperature seasonality (e.g. Wilkinson and Ivany, 2002; Goodwin et al., 2003; 2009; Judd et al., 2018). Due to the complexity added by variations of seasonal growth rate and environmental parameters, building accurate intra-annual chronologies requires high-resolution  $\delta^{18}\text{O}_c$  data (>20 samples/year; Goodwin et al., 2003). This makes such chronologies ineffective in terms of costs and time for studies targeting larger numbers (>10) of specimens, such as this one. Recent studies have shown that Mg/Ca ratios in oyster shells follow the seasonal temperature cycle (e.g. Surge and Lohmann, 2008; Ullmann et al., 2013; Mouchi et al., 2013), and that annual cycle counts in Mg/Ca profiles yield accurate, reproducible estimates of shell ages (Durham et al., 2017). The degree to which Mg/Ca in oysters is directly temperature-controlled is debated, with some studies obtaining significant temperature correlations only for part of the ontogeny (e.g. juvenile *Crassostrea gigas*: Mouchi et al., 2013; juvenile *Saccostrea glomerata*; Tynan et al., 2017; adult *Crassostrea virginica*: Surge and Lohmann, 2008). Others found rela-

tionships exclusively in the chalky (Ullmann et al., 2013) or foliated (Surge and Lohmann, 2008) microstructure. A more recent study sampling foliated calcite from the entire ontogeny in shells from multiple modern and fossil oyster species (including *C. gigas*) found that Mg/Ca seasonality is a highly successful tool for age determination (97% success rate; Durham et al., 2017). This forms the basis for Mg/Ca-based age modeling approach used here.

The correlation between Mg/Ca profiles and approximations by our age model ( $0.34 < r < 0.97$ ; with  $r \geq 0.7$  in 10 out of 12 specimens; Fig. 6) is equal to or better than Mg/Ca-temperature correlations reported in previous studies (e.g. Surge and Lohmann, 2008; Mouchi et al., 2013). Sub-annual (e.g. tidal/lunar) variability, which is known to influence Mg/Ca in *C. gigas* shells (Mouchi et al., 2013), or measurement uncertainty reduces the correlation in shorter records (e.g. H4 and O5). The consistent correlation between Mg/Ca and seasonality is confirmed by comparison with inter-annual  $\delta^{18}\text{O}_c$  profiles in specimens H1, M1 and M2 (see 2.9 and Supplementary Information). The modeling routine successfully approximates seasonal variability observed in Mg/Ca profiles throughout the ontogeny of our specimens by combining growth rate and seasonality sinusoids (Fig. 6) and corroborates previous work (e.g. Bougeois et al., 2014; Durham et al., 2017) in demonstrating that Mg/Ca profiles in *C. gigas* form a reliable basis for age determination. Since Mg/Ca profiles can be measured much more rapidly, at higher resolution and at lower cost using techniques like LA-ICPMS (e.g. Durham et al., 2017) and  $\mu\text{XRF}$  (de Winter and Claeys, 2016), age models based on Mg/Ca ratios potentially achieve more precise age models compared to those based on less densely sampled records.

#### 4.1.2. Growth stops

Most specimens experienced at least one growth reduction or cessation in their lifetime, but growth stops do not seem to be concentrated in a specific part of the year (Fig. 6). Since linear growth rate exhibits strong seasonality within specimens without a consistent phase relationship between specimens, linear growth rate likely depends on the local presence of calcite microstructures, which differs strongly per individual. It is therefore likely not a good measure for growth rates of the shell as a whole. The lack of consistency in the timing of growth stops corroborates previous results (e.g. Huyghe et al., 2019; de Winter et al., 2020a) arguing against a fixed lower temperature threshold for shell growth in oysters (e.g. Lartaud et al., 2010a; Ullmann et al., 2010). The significant difference in linear growth rates between foliated ( $33.0 \pm 4.3 \mu\text{m/d}$ ) and chalky ( $42.7 \pm 5.4 \mu\text{m/d}$ ) microstructures show that the presence of microstructures in the hinge region exerts a dominant control on local growth rates in the shell, which is in agreement with previous studies (e.g. Checa et al., 2018; Banker and Sumner, 2020) demonstrating that microstructural change helps the oyster to achieve plasticity in shell shape.

#### 4.1.3. Growth and mineralization rate

Our approach only allowed quantification of linear growth rates in measurement (and growth) direction. Given the complex shape of oyster shells, the  $\sim 30\%$  higher linear

growth rate of the chalky microstructure compared to foliated calcite may not directly translate to a higher calcite mineralization rate. Assuming growth rate differences between the microstructures are similar in all three dimensions, our result would translate to a  $\sim 2.2$ -fold increase volumetric growth rate in the chalky microstructure compared to the foliated microstructure:

$$\frac{\frac{dV}{dt} \text{ chalky}}{\frac{dV}{dt} \text{ foliated}} \approx \frac{\left(\frac{dL}{dt} \text{ chalky}\right)^3}{\left(\frac{dL}{dt} \text{ foliated}\right)^3} = \frac{42.7^3}{33.0^3} = 2.17$$

Considering the typical difference in density between chalky ( $1.15\text{--}1.32 \text{ g/cm}^3$ ; Chinzei, 1995) and foliated ( $2.2\text{--}2.5 \text{ g/cm}^3$ ; Chinzei, 1995; Yoon et al., 2003) microstructures, the actual difference in mineralization rate (in mass per unit time) is smaller. Unless the most extreme differences in density ( $1.15 \text{ g/cm}^3$  for the chalky and  $2.5 \text{ g/cm}^3$  for the foliated microstructure) are considered, mineralization rates for the chalky microstructure remain (up to 30%) higher than those of the foliated microstructure:

$$\frac{\frac{dM}{dt} \text{ chalky}}{\frac{dM}{dt} \text{ foliated}} = \frac{\rho_{\text{chalky}}}{\rho_{\text{foliated}}} * \frac{\frac{dV}{dt} \text{ chalky}}{\frac{dV}{dt} \text{ foliated}} = \frac{(1.15 - 1.32)}{(2.2 - 2.5)} * 2.17 \approx 1.0 - 1.3$$

Note that these rough calculations rely on simple assumptions and that a more thorough assessment of differences in mineralization rate would require information about shell growth rate and density variability in three dimensions. To improve on this estimate of mineralization rate differences between microstructures, we recommend that further research be done to quantify differences in secreted volume and density using micro computerized tomography (as in Banker and Sumner, 2020) or similar methods that resolve spatial differences in density in three dimensions. Nevertheless, it seems likely that the chalky calcite is mineralized at a faster rate than the foliated calcite.

#### 4.1.4. Microstructure transitions

Visible observation and light microscopy images suggest that lenses of chalky microstructure are strictly intercalated between folia, forming sharp boundaries with the foliated structure, and that they are chronologically separate (i.e. they do not form simultaneously). However, SEM close-ups of boundaries between microstructures show that transitions of foliated into chalky microstructures consist of gradual changes of orientation of calcite laths instead of sharp boundaries (Fig. 3D, G and H). The same is true for the transition from the chalky structure into the foliated structure, as is clear from the truncation of folia in the foliated structure on the boundary between microstructures (Fig. 3H). This truncation shows that the lenses of chalky structure close progressively over time. Similarly, in the case shown in Fig. 3H, precipitation of foliated on top of chalky calcite starts close to outer margin of the shell hinge and later occurs further away from the outer margin. These observations agree with detailed structural observations of the microstructures of *C. gigas* (Checa et al., 2018), micro-CT observations of *C. gigas* shells in three dimen-

sions (Banker and Sumner, 2020) and Mn-labeled isochrons cutting through multiple microstructures (Lartaud et al., 2010b) demonstrating that foliated and chalky calcite are deposited simultaneously in different parts of the shell of *C. gigas*. This also explains the lack of seasonal control on the formation of microstructures in *C. gigas* (see 3.5 and **Supplementary Information**). However, given the fast growth rate and highly localized nature of chalky lenses both in space and time, a sample of chalky microstructure might nonetheless be easily biased because it may be formed predominantly during one season.

#### 4.1.5. Implications for growth markers in oyster shells

Our clumped isotope temperature reconstructions (see 3.6) show that formation of the foliated microstructure is more concentrated in the warmer (summer) months than that of the chalky microstructure. Thick bands of foliated calcite in the shells of *C. gigas* are thus more likely to be formed during the warm (summer) season. This superficial correlation between microstructure, seasonality and shell chemistry is corroborated by the apparent presence of peaks in Mg/Ca (associated with higher temperatures, e.g. Surge and Lohmann, 2008; Mouchi et al., 2013; Tynan et al., 2017; see also section 4.4.4) with thicker foliated calcite bands (see Fig. 4A). However, the lack of seasonal control on microstructural growth (see 3.5) and the heterogeneity in microstructural expression between individuals from the same environment (see Fig. 2) cast doubt on the reliability of thick foliated layers as markers for annual growth, as suggested in previous studies (e.g., Harding and Mann, 2006). Note also that the correlation of peaks in Mg/Ca with thick foliated calcite bands is only observed in transect through the foliated structure (Fig. 4A) and that higher Mg concentrations in the chalky microstructure (see Fig. 5) distort the relationship between Mg/Ca and microstructure (Fig. 4C). Similar suggestions for dating other oyster species (e.g., *Ostrea edulis*; Richardson et al., 1993 and *Crassostrea virginica*; Kirby et al., 1998) based on the presence of microstructures should always be backed up with independent evidence such as chemical analysis, especially in fossil specimens (e.g., Kirby et al., 1998; Surge et al., 2001; Harzhauser et al., 2011; Durham et al., 2017; de Winter et al., 2018). Aside from chemical profiles, which may be resource- and time-consuming, more reliable estimates for oyster shell age are obtained by chemical labeling (Lartaud et al., 2010b), counting external growth lines on the resilifer (e.g. Kirby et al., 1998), counting of high-resolution daily and tidal growth increments revealed using cathodoluminescence (Huyghe et al., 2019) or annually-paced dark and light zonation in the foliated microstructure (Higuera-Ruiz et al., 2009). The latter is confirmed by our observations of dark and light zones in foliated calcite (see Fig. 3) correlating with seasonal variability in Mg/Ca ratios (see Fig. 6 and **Supplementary Information**).

## 4.2. Formation mechanisms of microstructures

The lack of seasonality in the expression of microstructure and the strong inter-specimen variability in the timing

of the occurrence of microstructures (Fig. 2) suggests that environmental variability plays a minor role in microstructure development. Full shell cross-sections (Fig. 2; samples O1-8) and micro-CT evidence (Banker and Sumner, 2020) demonstrate that the size and frequency of lenses of chalky structure vary widely within and between specimens. Lenses of chalky microstructure are highly local phenomena and their location in three dimensions in the shell depends strongly on the irregular morphology of the shell. While this leaves the question of microbial “remote mineralization” open, the stable isotope values results argue strongly against this hypothesis (Fig. 9). The two microstructures are very similar in all isotope systems studied ( $\delta^{13}\text{C}_c$ ,  $\delta^{15}\text{N}$ ,  $\delta^{18}\text{O}_c$  and  $\delta^{34}\text{S}$ ), with the only significant difference documented in  $\delta^{18}\text{O}_c$ . The latter is explained by strong inter-specimen variability in the microsampled specimens H1, M1 and M2 due to the large effect of temperature seasonality on  $\delta^{18}\text{O}_c$  (see Fig. 8 and Fig. 9). Similarly, seasonal sampling biases, especially in the fast-growing and relatively short-lived chalky lenses, also explain oxygen isotopic differences between microstructures in some specimens (e.g. H1, M1 and M2; see also **Supplementary Information**), which are averaged out in intra-specimen means. If precipitation of the chalky microstructure was mediated by sulphate-reducing bacteria (as suggested in Chinzei and Seilacher, 1993, and Vermeij, 2014), the  $\delta^{34}\text{S}$  value of the resulting carbonate would be much higher (Brunner et al., 2005), resembling those of dissolved sulphate in areas of the modern ocean where bacterial sulphate reduction (BSR) presently takes place (e.g. ‘Black Spots’ in coastal waters,  $\delta^{34}\text{S} = 35\text{--}45\text{‰}$ ; Böttcher et al., 1998). Instead, the  $\delta^{34}\text{S}$  composition of both chalky and foliated microstructures in *C. gigas* are not statistically different from that of dissolved sulphate in well-oxygenated North Sea water ( $\delta^{34}\text{S} = 20\text{--}21\text{‰}$ ; Böttcher et al., 2007) and oxygenated pore water in surface sediments in the North Sea ( $\delta^{34}\text{S} = 20.5\text{--}22\text{‰}$ ; Böttcher et al., 2007). Their sulfur isotope values resemble carbonate-associated sulphate in other shell-producing fauna (mollusks and brachiopods) growing under very similar oxic conditions in which no BSR contribution is suspected ( $\delta^{34}\text{S} = 21\text{--}22\text{‰}$ ; Richardson et al., 2019). The close agreement between  $\delta^{34}\text{S}$  in *C. gigas* and dissolved  $\delta^{34}\text{S}$  in its direct environment shows that both microstructures in oyster shells are reliable recorders of  $\delta^{34}\text{S}$  of environmental sulphate and, like foraminifera, can be used as archive for changes in  $\delta^{34}\text{S}$  over geological history (Rennie et al., 2018).

Likewise, the similarity of the average  $\delta^{15}\text{N}$  and  $\delta^{13}\text{C}_c$  values in the chalky and foliated calcite suggest that in *C. gigas* the two structures are formed by the oyster without pronounced microbial interference. Given the complex interplay of processes that contribute to the N inputs in the North Sea, including river discharge, atmospheric deposition, nutrient consumption and sediment–water fluxes, and their spatial and temporal variability (Rolf et al., 2008; Dähnke et al., 2010), evaluating the isotopic composition of the oyster N source is, at this point, challenging and requires further investigation. Oyster calcite ( $\delta^{15}\text{N}_{\text{chalky}} = 13.5\text{--}14\text{‰AIR}$ ;  $\delta^{15}\text{N}_{\text{foliated}} = 12.5\text{--}15\text{‰AIR}$ ; Figs. 8 and 9; Table 3 and **Supplementary Information**)



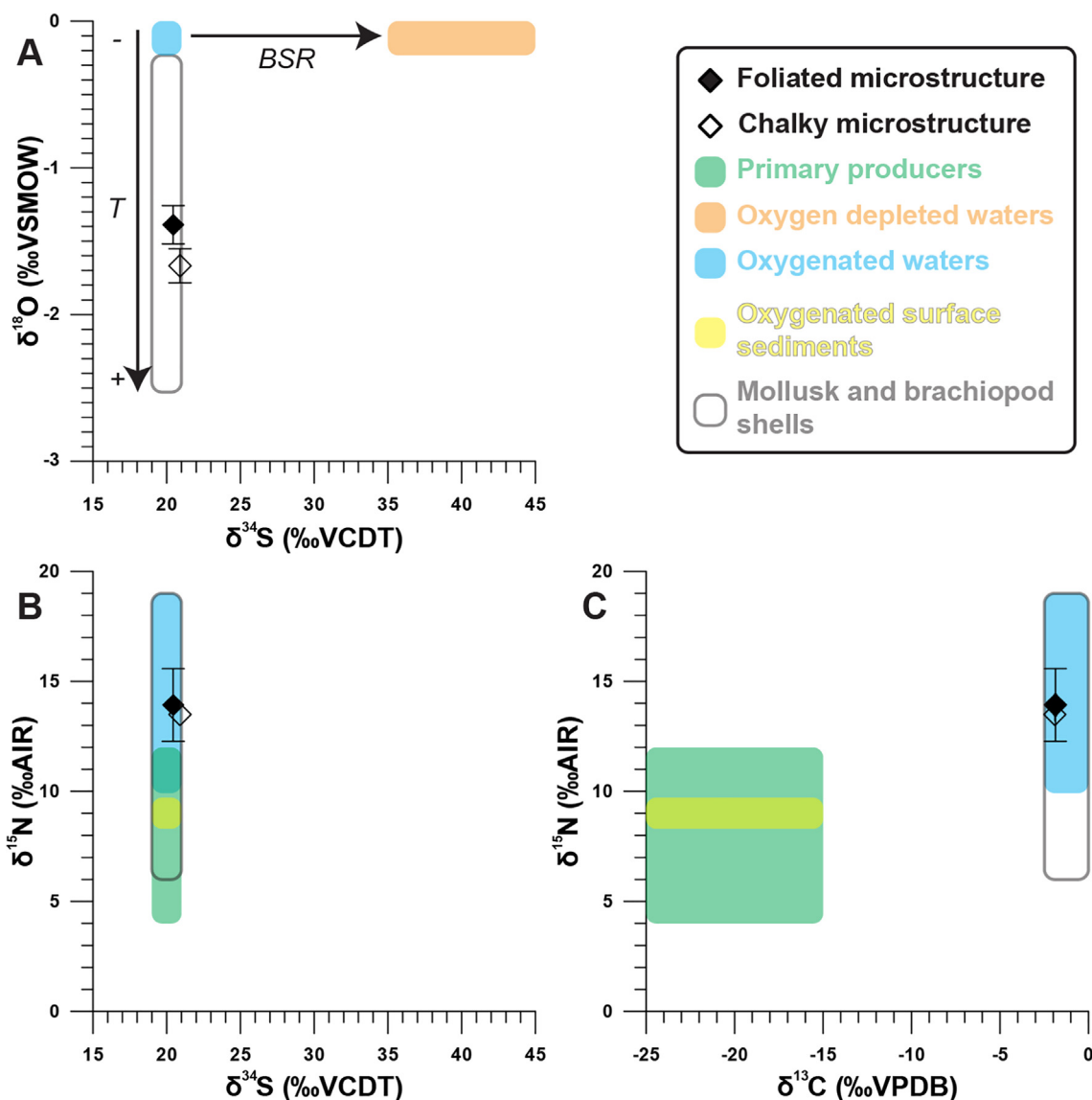


Fig. 9. Cross plots of (A)  $\delta^{18}\text{O}_c$  against  $\delta^{34}\text{S}$ , (B)  $\delta^{15}\text{N}$  against  $\delta^{34}\text{S}$  and (C)  $\delta^{15}\text{N}$  against  $\delta^{13}\text{C}_c$  showing average stable isotopic compositions of calcite in the foliated (closed symbols) and chalky (open symbols) microstructure of *C. gigas* compared to the stable isotopic compositions of various compounds in the modern environment taken from the literature: Stable isotope compositions of primary producers from Salomons and Mook, 1981, Stribling and Cornwell, 1997, Pättsch et al., 2010. Stable isotope compositions from oxygen depleted waters from Böttcher et al., 1998, Voss et al., 2005 and Rolff et al., 2008; Bourbonnais et al., 2015. Compositions of well oxygenated waters and oxygenated surface sediments: Salomons and Mook, 1981, Böttcher et al., 1998 and Pättsch et al., 2010. Compositions of shells of mollusks and brachiopods: Ullmann et al., 2013, Gillikin et al., 2017 and Richardson et al., 2019. The black arrow in A indicates the direction in which Bacterial Sulfate Reduction (BSR) would change the composition of the calcification fluid and resulting shell material.

shows a 4.5 to 5.5‰ enrichment in  $^{15}\text{N}$  with respect to coastal seawater nitrate and particular organic matter, which has been reported to be around 8 – 9‰ in the North Sea German Bight, i.e. the closest nitrate  $\delta^{15}\text{N}$  data available (Dähnke et al., 2010). Shell-bound  $\delta^{15}\text{N}$  is somewhat higher than the expected 3–4‰ enrichment per trophic level elevation (DeNiro and Epstein, 1978; Schoeninger & DeNiro, 1984) Together with the ~ 2.5‰  $\delta^{15}\text{N}$  variability observed between foliated calcite samples, this either suggests that *C. gigas* takes in nitrogen from various sources and different trophic levels while filter feeding (as observed in the bivalve *Rangia cuneata*; Graniero et al., 2021) or

possibly reflects some degree of biological control on nitrogen incorporation into shell-bound organic matter. Note that the thorough preparation method for mineral-bound organic matter  $\delta^{15}\text{N}$  analyses excludes the possibility that salt and fluid inclusions in the microstructures affect the  $\delta^{15}\text{N}$  result. The complex processes that govern nitrogen uptake and incorporation into the shell require more detailed investigation, but the similarity in  $\delta^{15}\text{N}$  between microstructures argues against microbial interference.

Carbon isotope values from chalky microstructures ( $\delta^{13}\text{C}_c = -1.91 \pm 0.09$ ‰ VPDB) are indistinguishable from those of the foliated microstructure ( $-1.87 \pm 0.05$ ‰ VPDB).

These values agree more closely with the isotopic composition of dissolved inorganic carbon in well-oxygenated waters (e.g., North Sea;  $\delta^{13}\text{C}_c = -1.5$  to  $0$  ‰VPDB; Salomons and Mook, 1981) than the more depleted values in oxygen-depleted waters (e.g. Baltic Sea floor;  $\delta^{13}\text{C}_c = -4$  to  $0$  ‰VPDB, Voss et al., 2005), where the conditions for BSR are met. Carbon in the shell is likely predominantly derived from DIC and partly by the diet of the oyster, with a positive trophic fractionation factor (+2 to 4‰; DeNiro and Epstein, 1978; McConnaughey and Gillikin, 2008). The  $\delta^{13}\text{C}_c$  values in *C. gigas* microstructures indeed reflect this offset relative to  $\delta^{13}\text{C}$  in well-oxygenated waters, arguing against the hypothesis that conditions allowing BSR to take place prevailed in the extrapallial fluid from which the chalky microstructure formed. Note that strong metabolic effects on  $\delta^{13}\text{C}_c$  complicate a direct relationship with environmental conditions (McConnaughey and Gillikin, 2008).

The isotopic similarity observed between microstructures provides strong evidence against the “remote mineralization” hypothesis and corroborates findings in previous studies suggesting that both microstructures are formed by the oyster itself (Checa et al., 2018; Banker and Sumner, 2020). In addition, our microscopic observations show smooth microstructural transitions like those described in these previous studies (Fig. 3) and a significantly higher linear growth rate in the chalky microstructure (see 3.3 and Supplementary Information). These observations strengthen the hypothesis that physiological processes such as shell plasticity, growth stress and breakage of the periostracum determine the location and size of pockets of chalky microstructure in the shell of *C. gigas*. It therefore seems likely that the chalky structure is an adaptation of oysters to increase their shell growth rate temporarily and locally and produce irregular shells to accommodate irregularities on the surface of their substrate and limited space in their growth environment (as proposed by Checa et al., 2018; and Banker and Sumner, 2020). Note that our results leave room for further investigation into the precise mechanisms that allow oysters to control their shell microstructures to such a degree. While these findings likely have implications for chalky microstructures observed in related oyster species (e.g. *Crassostrea virginica* or *Ostrea edulis*; Korrington, 1951; Carriker et al., 1980), different porous microstructures in other bivalve taxa, such as the vesicular structure in foam oysters (Gryphaeidae; Stenzel, 1971) may have a different formation pathway which requires independent investigation.

### 4.3. Trace element partitioning

#### 4.3.1. Empirical distribution coefficients

The significant differences in trace element concentrations between microstructures (see Fig. 5) in absence of environmental control on microstructure formation (see 4.2) suggest an internal, rather than environmental, origin for microstructural differences. Internal or biological processes (“vital effects”), unrelated to the environment, have been shown to influence shell chemistry in a wide range of bivalve taxa (e.g. Lorrain et al., 2005; Wanamaker

et al., 2008; Schöne et al., 2011; Ullmann et al., 2013). Internal control on trace element composition is also evident from the lack of seasonality in empirical distribution coefficients (see 3.5 and Supplementary Information) and the difference between distribution coefficients in shell microstructures and inorganic calcite for all elements except Sr (Fig. 7). Relative to inorganic calcite, *C. gigas* discriminates more strictly against the incorporation of Mg and preferentially incorporates Na and S into its shell (Fig. 7). Unfortunately, no Cl distribution coefficient between inorganic calcite and water was found in the literature, but given its negative charge it is likely that Cl substitution in the carbonate matrix is likely very rare and the Cl distribution coefficient should be low (Ichikuni, 1983), in agreement with our observations in Fig. 7.

Trace element distribution coefficients into carbonate minerals have been the subject of several studies and have been found to depend on temperature, mineralization rate and the mineral formation pathway (direct precipitation from the fluid or remineralization from a precursor mineral; e.g. Morse and Bender, 1990; Rimstidt et al., 1998; Malone and Baker, 1999; Stoll et al., 2002; Gaetani and Cohen, 2006; Tang et al., 2008; Day and Henderson, 2013 and references therein). Given the lack of consensus in these studies regarding the temperature dependence of  $D_{\text{Sr}}$ , the lack of seasonality in oyster  $D_{\text{Sr}}$  does not exclude equilibrium for incorporation of Sr, but differences in Sr concentration between microstructures (see Fig. 4; Supplementary Information) likely reflect some degree of internal control despite the close similarity between our empirical distribution coefficients and literature values (e.g. Rimstidt et al., 1998; Day and Henderson, 2013). Note that the slightly lower Sr/Ca values we observe in the chalky microstructure are in contrast with previous observations of slightly higher Sr/Ca ratios in the chalky structure of *C. gigas* compared to the foliated structure (Ullmann et al., 2013). However, contrary to this study, Ullmann et al. (2013) did not compare time-equivalent chalky and foliated samples, making it harder to compare these results with ours. Nevertheless, these previous authors reached the same conclusions as this study, namely that oysters likely exert some degree of control on the Sr/Ca in their shells. Since our empirical distribution coefficients are based on differences between seawater and the entire oyster biomineral, they combine the result of all processes involved in shell formation. These include microstructural differences in mineralization rate, efficiency of the Ca pump controlling the composition of the extrapallial fluid and trace elemental concentrations outside the calcite mineral lattice.

#### 4.3.2. Effect of mineralization rate

Differences in linear growth rate between microstructures suggest a higher mineralization rate for the chalky microstructure, even after correction for differences in porosity (see 4.1.3). Higher mineralization rates are thought to increase the distribution coefficients of some elements (e.g. Mg and Sr) and decrease the distribution coefficient in others (e.g. Mn), while the effect is unresolved in Na, Cl and S (Lorenz, 1981; Rimstidt et al., 1998; Stoll et al., 2002; Tang et al., 2008). It has been demonstrated that

there exists a logarithmic relationship between calcite precipitation rate and trace element distribution coefficient (Lorens, 1981; Rimstidt et al., 1998; Tang et al., 2008). This relationship is explained by the formation of a solution boundary layer at the crystal-solution interface which enhances or reduces the concentration of trace elements in the solution close to the crystal surface (Surface Entrapment Model, see discussion in Watson and Liang, 1995; Rimstidt et al., 1998). Since the slope of this logarithmic relationship between distribution coefficient and mineralization rate is generally in the order of 0.2–0.3 for divalent cations (Lorens, 1981; Tang et al., 2008), we can estimate that the ~30% upper limit of the difference in secretion rate between chalky and foliated microstructures estimated in 4.1.3 accounts for a difference in distribution coefficient of at most ~8%:

$$\log D \leq 0.3 * \log R$$

$$\delta D \leq 10^{0.3 \pm 0.05 * \log 1.30} = 1.08$$

Here,  $D$  is the distribution coefficient,  $R$  is the mineralization rate, the slope between  $\log(D)$  and  $\log(R)$  is assumed to be 0.3 and the term “1.30” indicates a 30% increase in mineralization rate in the chalky microstructure compared to the foliated structure. Therefore, differences in empirical distribution coefficients (Fig. 7) cannot be explained by mineralization rate variability alone. In addition, the faster-growing chalky structure has a lower  $D_{Sr}$  than the foliated microstructure, opposite to the expected mineralization rate effect. Note that an opposite difference in  $Sr$  concentration between microstructures was observed by Ullmann et al. (2013), which may be explained by changes in mineralization rate (see 4.3.1). In addition, mineralization rate differences cannot explain the large differences in Na, Cl and S concentrations between microstructures.

#### 4.3.3. Rate-dependent ion transport

Alternatively, differences in trace element composition between microstructures can be a result of differences in the extrapallial fluid from which the shell mineralizes. These differences can be explained through the mineralization rate-dependent ion transport model (Carré et al., 2006). The  $Ca^{2+}$ -pump in mollusks adds Ca to the extrapallial fluid, but discriminates actively against other ions, such as Mg and Sr, which may cause impurities in the shell carbonate (Hagiwara and Byerly, 1981; Klein et al., 1996). At higher mineralization rates the  $Ca^{2+}$ -gradient between the calcification site and the outer epithelia increases, causing the  $Ca^{2+}$ -pump to discriminate less readily against non- $Ca^{2+}$  ions. The transport of divalent cations with electrochemical properties similar to  $Ca^{2+}$  (e.g.  $Mg^{2+}$ ,  $Sr^{2+}$  and  $Ba^{2+}$ ) through Ca-channels is well-documented (e.g. Hagiwara and Byerly, 1981). When fast biomineralization rates increase the electrochemical potential across the membrane, Ca and other cations can more easily enter the extrapallial fluid. Since the concentrations of Na, Mg, S and Cl are high in seawater (Pilson, 2012), these ions will be diffused into the extrapallial fluid at much higher rate than through the  $Ca^{2+}$ -pumping pathway due to the comparatively high concentration gradient between sea water and the extrapallial fluid. This increases the empirical distribution coefficient of elements

with high marine concentrations in fast growing biogenic carbonates (Carré et al., 2006). Interestingly, concentrations of Na, Mg, S and Cl in the chalky structure are always closer to the marine concentrations than those in the foliated structure (i.e., empirical distribution coefficient closer to 1; see Fig. 7; Table 2). This process can explain why *C. gigas* cannot discriminate against these common ions as effectively in the fast-growing chalky microstructure as compared to the slower growing foliated microstructure. It must be noted that some previous authors found no observable difference between body fluids (including extrapallial fluid) of marine mollusks and surrounding waters (Onuma et al., 1979), casting doubt on this hypothesis. However, it remains a possibility that spatial differences in fluid chemistry occur within the animal.

#### 4.3.4. Non-lattice-bound elements

Since our XRF method analyzed trace elements in the entire biomineral, the contribution of elements associated with organic matter or in fluid inclusions must be considered. It seems plausible that the larger porosity of the chalky microstructure allows for higher amounts of salt and fluid inclusions in the shell structure. This could partly explain why concentrations of Na, Mg, S and Cl are higher in the chalky structure (see Fig. 5; Table 2) and why Na and Cl co-vary on the microscale (Fig. 4). However, the mass proportions of Na and Cl in oyster calcite ( $[Na]/[Cl] \approx 0.3$ ; Figs. 4 and 5) differ from those of sea water ( $[Na]/[Cl] \approx 0.9$ ; Pilson, 2012) and Mg and S do not follow the same pattern on the microscale, suggesting that salt and seawater inclusions can only partly explain the observed variability in these elements. In addition, recent models for oyster shell formation, do not support direct exchange between shell porosity and seawater (Banker and Sumner, 2020). Nevertheless, the possibility that fluid and/or sea salt inclusions partly explain compositional differences between microstructures cannot be excluded.

Organic matrices in carbonate biominerals are known to contain significant quantities of trace elements (Lorens and Bender, 1980; Takesue et al., 2008; Schöne et al., 2010; Geerken et al., 2019). The concentration of some elements, most notably sulfur, in the organic matrix can exceed that contained in the mineral part of the shell (Takesue et al., 2008; Schöne et al., 2010), while other elements (e.g. Sr and Ba) are almost exclusively found in the mineral fraction of the shell (Takesue et al., 2008). The covariation of Mg and S in the profiles through mixed microstructures (Fig. 4C) suggests a common cause for microstructural differences in concentrations of these elements which may be related to association with organic matrix (Dauphin et al., 2003; England et al., 2007). However, closer inspection shows that this correlation is not consistent between specimens (Fig. 5). Furthermore, there is no indication for a factor 2–3 difference in organic matter concentration between microstructures required to explain the large differences in S and Mg between microstructures within specimens. Given the high affinity of some elements with the organic matrices of bivalve shells (e.g. Takesue et al., 2008; Schöne et al., 2010), any differences in organic matter content between microstructures are expected to affect trace element concentrations. To test whether differ-

ences in organic matter content explain a significant fraction of the compositional differences between microstructures trace element content should be analyzed in microstructure samples before and after oxidative cleaning (*sensu* Takesue et al., 2008; Schöne et al., 2010).

#### 4.4. Implications for oyster shells as archives for environmental change

##### 4.4.1. Kinetic effects

Our rejection of the “remote mineralization” hypothesis for the chalky structure in *C. gigas* strongly suggests that stable isotope ratio analyses of chalky and foliated calcite that grew simultaneously should have a similar isotopic composition. Since differences in mineralization rate between the microstructures are likely, isotope data should nevertheless be interpreted with care, as these have been demonstrated to cause kinetic fractionation which may significantly change isotope ratios in fast-growing biominerals (Owen et al., 2002; Bajnai et al., 2018; Daëron et al., 2019 and references therein). Small isotopic differences between microstructures have been observed in other bivalve taxa (e.g., *Arctica islandica*; Trofimova et al., 2018). However, a large number of studies show that bivalve shells are generally precipitated at (or close to) oxygen isotope equilibrium (e.g. Surge et al., 2001; Schöne et al., 2005b; Ullmann et al., 2010 and references therein). Within this study, we did not find a significant difference in isotopic composition that can be explained by difference in microstructure. However, differences in average growth rate between chalky ( $42.0 \pm 5.2 \mu\text{m/d}$ ) and foliated microstructure ( $33.0 \pm 4.2 \mu\text{m/d}$ ) and associated estimates of mineralization rate differences are small (up to 30% higher in the chalky structure, see 4.1.3), so this observation alone does not rule out the influence of kinetic effects. While kinetic effects are known to cause departure from carbonate (oxygen and clumped) isotope equilibrium in brachiopods (Bajnai et al., 2018), bivalves have different biomineralization pathways so this result may not apply to *C. gigas*.

##### 4.4.2. Seasonality bias

A possible explanation for the difference in  $\delta^{18}\text{O}_c$  and  $\Delta_{47}$  between the microstructures is a difference in the timing of their formation. The fast (compared to the foliated microstructure) and local mineralization of lenses of chalky calcite together with seasonal influence on shell growth (see 3.5) in the shell may cause biases towards different seasons in  $\delta^{18}\text{O}_c$  and  $\Delta_{47}$  samples between microstructures. In specimens microsampled for  $\delta^{18}\text{O}_c$  (e.g. H2 and M2) this bias is evident from the more even spread in  $\delta^{18}\text{O}_c$  values in the foliated microstructure than the chalky microstructure (Fig. 8). Averaging  $\Delta_{47}$  values within bulk samples before converting them to temperature reconstructions prevented biasing the averages towards higher temperatures due to the non-linear  $\Delta_{47}$ -temperature relationship ( $\Delta_{47} \frac{1}{T^2}$ ; Bernasconi et al., 2018). The effect of this non-linear relationship on homogenizing shell samples grown under different conditions is  $< 0.3 \text{ }^\circ\text{C}$  given the seasonal temperature variability in the sample localities and cannot explain the offset of  $\Delta_{47}$ -based temperature reconstructions from the

mean annual temperatures (Fig. 8 see **Supplementary Information**). We conclude that the specific chalky lenses sampled in specimens M2 and M6 formed under cooler, lower- $\delta^{18}\text{O}_c$  (spring) conditions compared to the bulk of the foliated microstructure (Fig. 8). Plots of growth rate through mixed microstructure profiles plotted against time of shell formation indeed show that chalky lenses form predominantly in spring and autumn (**Supplementary Information**). Based on the observed differences in (linear) growth rate between microstructures and the age model, we find that the foliated microstructure develops at conditions of no more than  $1.5 \text{ }^\circ\text{C}$  warmer than the chalky microstructure (see **Supplementary Information**). This difference is only observed in some specimens and does not explain the  $\sim 5 \text{ }^\circ\text{C}$  difference observed between the microstructures based on  $\Delta_{47}$  measurements. Instead, the most likely explanation is that the short-lived nature of chalky lenses and the lack of seasonal control on microstructure formation precludes drawing meaningful conclusions about the timing of mineralization or environmental conditions from bulk measurements in this microstructure.

Dominant summer influence on foliated calcite formation likely explains the lower  $\Delta_{47}$  and higher  $\delta^{18}\text{O}_w$  results because summers are characterized by higher SSS and  $\delta^{18}\text{O}_w$  (see Fig. 8 and **Supplementary Information**). However, it should be noted that kinetic effects on  $\Delta_{47}$  and  $\delta^{18}\text{O}_c$  results cannot be fully excluded and require further investigation (e.g. through the new dual  $\Delta_{47}$ - $\Delta_{48}$  clumped isotope method; Bajnai et al., 2020). Note that the difference in  $\delta^{18}\text{O}_w$  is not statistically significant and direct comparison of bulk isotopic values with environmental  $\delta^{18}\text{O}_w$  and SST is complicated by large seasonal variability in the environment (see 3.6; Fig. 8 and **Supplementary Information**). Our data shows that growth of *C. gigas* varies seasonally, as was observed in previous studies (e.g. Ullmann et al., 2010; Mouchi et al., 2013). Avoiding this bias requires seasonally resolved  $\Delta_{47}$  records to be compared to temporally aligned *in situ* SST records, rather than to the annual average, which may not be representative of the calcification temperature due to seasonal bias (see de Winter et al., 2020b). Our results corroborate previous studies demonstrating that seasonal bias in bulk samples of mollusk shell carbonate can significantly affect the accuracy of mean annual SST reconstructions (e.g. Goodwin et al., 2003; Lartaud et al., 2010a; Judd et al., 2020). Reconstructions based on seasonally resolved proxy records should be preferred over bulk sampling for such reconstructions.

##### 4.4.3. Implications for sampling strategies

Linear growth rates vary strongly between individuals and the difference in growth rate between microstructures is larger in the samples from Texel (TH and MB) than in those from Brittany (BR; Fig. 6; S11). The intertidal locality may explain the higher variability in growth rate in the Texel specimens. Sudden changes in growth rate throughout the shells of oysters are hard to isolate without the use of detailed, sub-annual scale shell chronologies, such as those based on daily and tidal growth increments (e.g., Huyghe et al., 2019). Therefore, chemical records that cross multiple microstructures should be interpreted with care to

avoid growth rate-related biases, such as those discussed in 4.3. We recommend that such proxies are developed and applied separately for different microstructures. The lack of environmental influence on microstructural development (see 3.5), the lack of sharp, isochronous boundaries between microstructures (see Fig. 3 and Lartaud et al., 2010b) and the limited prevalence of growth cessations (see 3.3; Fig. 6 and Supplementary Information) strongly suggest that sampling the chalky microstructure can be avoided without compromising coverage of a chemical time-series from *C. gigas* shells. This sampling strategy limits the risk of biasing part of the record used for environmental monitoring or reconstructions by including multiple microstructures. This is important for studies of fossil oyster shells because previous studies have demonstrated that porous microstructures in oysters are more susceptible to diagenetic alteration, which may compromise recovery of the original chemical signature (e.g., de Winter et al., 2018).

#### 4.4.4. Implications for trace element proxies

The fact that differences in elemental incorporation remain even when controlling for environmental variables (see 3.4 and 3.5) is problematic for the development of trace element proxies in oyster and other bivalve shells. Our results confirm previous findings demonstrating the effect of mineralization rate on trace element incorporation in bivalve shells (e.g. Lorrain et al., 2005; Gillikin et al.,

2005; Freitas et al., 2006; Ullmann et al., 2013). This effect is stronger in chalky microstructure, where growth rates are higher and more variable, but we cannot fully exclude a growth rate effect on element concentrations in the foliated microstructure. The difference between estimated distribution coefficients and those for inorganic calcite illustrate that *C. gigas* exerts a strong biological control (“vital effect”) on incorporation of these elements in its shell. Considering that oyster calcite is comparatively low in Mg and Sr compared to other biogenic calcites (Dodd, 1967), the biological control seems comparatively strong on Mg and less so on Sr incorporation (see also Fig. 7). The incorporation of Sr into the shell of *C. gigas* seems to happen close to equilibrium, but our results show that distribution coefficients of Sr in *C. gigas* have no seasonal component and differ significantly between localities. Previous work on oysters (e.g. Ullmann et al., 2013) and other bivalves (e.g. Lorrain et al., 2005; Gillikin et al., 2005; Freitas et al., 2006) showed that Sr/Ca is controlled by metabolic processes. Future work exploring Sr/Ca ratios as environmental proxy in oyster shells should therefore be cautious to isolate effects of metabolic or mineralization rate.

The lack of consensus between transfer functions for Mg/Ca in oyster shells (Fig. 10 and e.g., Surge and Lohmann, 2008; Ullmann et al., 2013; Mouchi et al., 2013; Tynan et al., 2017) reflects variability in distribution coefficients due to local differences in environmental condi-

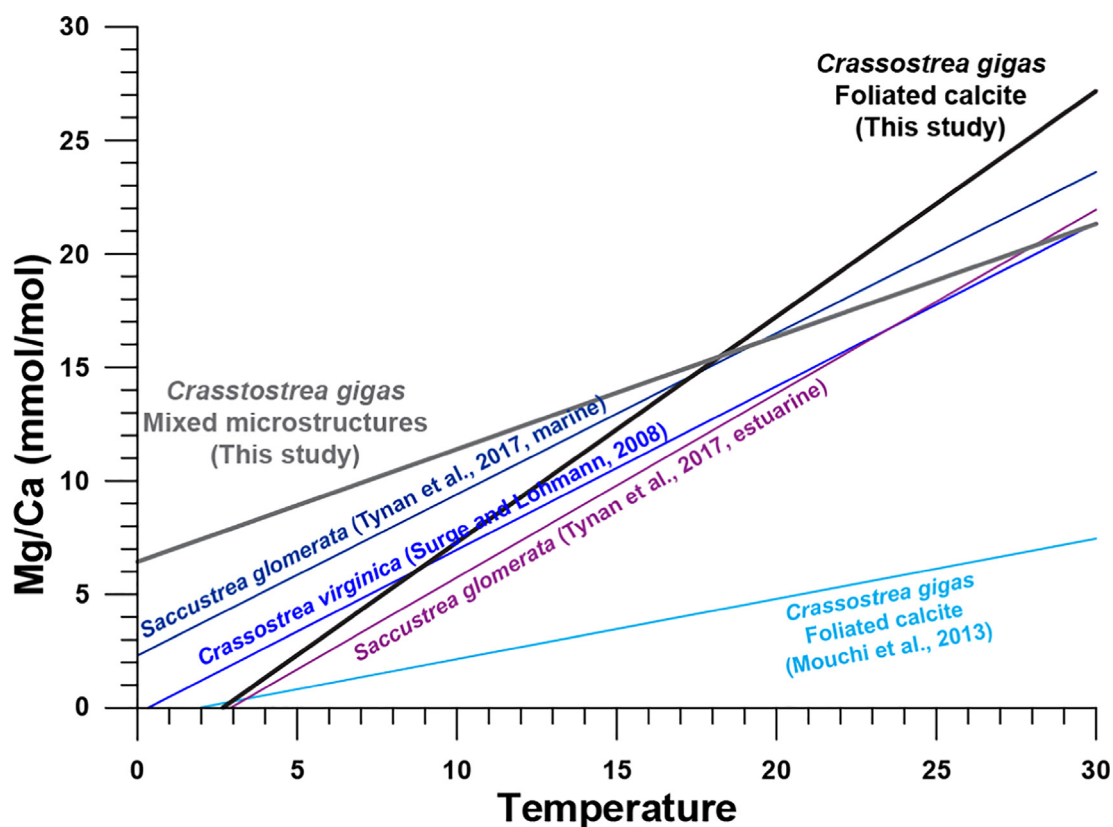


Fig. 10. Comparison of regressions between Mg/Ca in oyster shells and temperature. Colored lines show regressions constructed by previous authors (Surge and Lohmann, 2008; Mouchi et al., 2013; Tynan et al., 2017). Bold lines show regressions based on data from specimens O4, O8 and M6 based on measurements in foliated microstructure only (black;  $\text{Mg/Ca}_{\text{shell}}[\text{mmol/mol}] = 0.99 \cdot T[^\circ\text{C}] - 2.64$ ) or lines through both foliated and chalky microstructure (gray;  $\text{Mg/Ca}_{\text{shell}}[\text{mmol/mol}] = 0.50 \cdot T[^\circ\text{C}] + 6.44$ ).

tions or mineralization rate (Fig. 7) or a lack of a robust relationship between Mg/Ca and temperature. However, the similarity between Mg concentrations and distribution coefficients between localities in this study (Figs. 5 and 7; Table 1) and the strong seasonal variability found in oyster Mg/Ca ratios (see Figs. 4 and 6 and Section 3.5; e.g. Ullmann et al., 2013; Mouchi et al., 2013; Durham et al., 2017; Bougeois et al., 2018) likely reflects a real imprint of environmental change on shell chemistry, which can be used to reliably link shell growth to the annual cycle. This seasonality in Mg/Ca has in some cases been shown to diminish after the first two growth years due to a decrease in growth rate (Mouchi et al., 2013), but previous work on *C. virginica* (Durham et al., 2017) and Mg/Ca profiles in this study (Fig. 6) show that annual cycles can be resolved in later growth years and used as a basis for age modeling. The comparatively strong seasonal component observed in  $D_{Mg}$  (see 2.5) and good correlations between Mg/Ca and the seasonality-based age model approximations (Fig. 6) show that Mg/Ca seasonality can be resolved in *C. gigas* despite the imprint of higher frequency variability in SST and/or Mg concentrations in the extrapallial fluid on the high resolution  $\mu$ XRF Mg/Ca profiles related to natural or circadian daily and tidal variability (see de Winter et al., 2020d; **Supplementary Information**). Sub-annual variability is more easily resolved in fast-growing shell portions, partly explaining the weaker correlations between Mg/Ca and SST in profiles incorporating the fast-growing chalky microstructure. In specimens with strong Mg/Ca seasonality (O4, O8 and M6; see **Supplementary Information**), the slope of the Mg/Ca-temperature correlation for foliated calcite ( $Mg/Ca_{shell}[mmol/mol] = 0.99 * T[^\circ C] - 2.64$ ) resembles relationships found for *C. virginica* (Surge and Lohmann, 2008) and *Saccostrea glomerata* (Tynan et al., 2017). The *C. gigas* calibration by Mouchi et al. (2013) more closely resembles the regression obtained from including the chalky microstructure in this study ( $Mg/Ca_{shell}[mmol/mol] = 0.50 * T[^\circ C] + 6.44$ ; Fig. 10), even though Mouchi et al. (2013) based their calculations solely on measurements of foliated microstructures. This may be explained by the fact that the calibration by Mouchi et al. (2013) was based on (<1 year old) juvenile *C. gigas* specimens which exhibited higher growth rates, much like the chalky microstructure. Note that, contrary to observations in this study, Mouchi et al. (2013) did not find a significant Mg/Ca-temperature relationship for adult specimens of *C. gigas*. The differences in the slope and significance of the Mg/Ca-temperature relationships between studies may be attributed to site-specific differences in water chemistry and growing conditions (e.g. salinity and food availability) which may influence the Mg uptake and growth rate in oysters.

Given these findings in the context of the great variability in growth rate within oyster shells (due to their plasticity, see Banker and Sumner, 2020), between individuals (see **Supplementary Information**) and between localities (e.g., Lartaud et al., 2010a), the likelihood that one universal proxy transfer function can be developed linking Na, Mg, S or Mn concentrations to environmental variables seems small, even when only one microstructure (e.g. the foliated

calcite only) is included. One potential solution that should be explored is to incorporate local growth or biomineralization rate as a variable in transfer functions of trace element proxies to isolate its effect. Doing so would require the effect of growth rate on the distribution coefficient of elements into the shell to be quantified by growing bivalve species under controlled conditions and manipulating their growth rate (e.g. by varying food concentrations). This study shows that empirical elemental distribution coefficients between shell carbonate and seawater are a valuable tool for evaluating the potential for element concentrations in biogenic carbonates to record environmental variability, and to quantify vital effects in trace element proxies.

## 5. CONCLUSIONS

A combination of microscopy, stable isotope analyses and elemental analysis on 18 specimens of *Crassostrea gigas* from coastal waters in the Netherlands and France reveals that the chalky microstructures in oysters are not formed via microbially assisted carbonate mineralization, as previously proposed. Foliated and chalky calcite structures are similar with respect to carbon, nitrogen, and sulfur isotope ratios, and show only a minor difference in oxygen isotopic composition. The latter is likely a result of sampling bias given the strong influence of temperature seasonality on the oxygen isotopic compositions in mollusk shells. We observe that clumped isotope analyses on bulk samples of oyster calcite overestimate the mean annual temperature in which the organisms grew, likely due to seasonal sampling bias. The overestimation is significantly smaller for the chalky calcite (+3.8 °C) than for the foliated calcite (+8.5 °C). Detailed shell chronologies based on high-resolution Mg/Ca records corroborate previous work in showing that the presence of different microstructures is not linked to environmental changes and suggest that the chalky microstructure can be left unsampled for chemical profiles without introducing hiatuses in the record. Because chalky microstructures in *C. gigas* are characterized by higher and more variable calcification rates, including them may introduce bias in reconstructions and environmental monitoring using proxy records from oyster shells. We therefore recommend sampling the foliated over the chalky microstructure for clumped isotope analysis and strongly recommend that seasonality in temperature and growth rate is considered in oyster sclerochronology studies to prevent sampling bias.

Element distribution coefficients between oyster calcite and seawater show that oysters exert a strong influence on the incorporation of elements into their shells. Variability in mineralization rates, biologically controlled concentrations of the extrapallial fluid and inclusions of seawater, salt, and organic matter influence trace element concentrations in the biomineral. Despite these issues, Mg/Ca ratios in our specimens vary seasonally and show temperature sensitivities like those found in previous studies. We show that, regardless of whether this temperature dependence reveals a robust mechanistic process and can be used as a paleoproxy, high-resolution Mg/Ca profiles form a reliable basis for age modeling in oyster shells.

Our results show that there is little promise for the development of universal trace element proxy transfer functions for bivalve shells unless detailed shell chronologies can be used to correct for changes in calcification rates and the internal mechanisms of bivalve shell biomineralization from the extrapallial space are better understood. Future research should reveal whether the distribution coefficients of elements into the shells of other mollusk species show similar patterns and whether the effect of mineralization rates on element incorporation into bivalve shells is universal.

### Declaration of Competing Interest

The authors declare that they have no known competing financial interests or personal relationships that could have appeared to influence the work reported in this paper.

### ACKNOWLEDGEMENTS

NdW is funded by a Marie Skłodowska Curie Individual Fellowship by the European Commission (843011-UNBIAS) and a Junior Postdoc Fellowship by the Flemish Research Council (FWO; 12ZB220N). GJR and LKD acknowledge funding from the Netherlands Earth System Science Center (NESSC; grant no. 024.002.001) from the Dutch Ministry for Education, Culture and Science (gravitation grant no. NWO 024.002.001). BRS gratefully acknowledges funding by the Deutsche Forschungsgemeinschaft (DFG; SCHO793/20+23). SG acknowledges support by the Belgian Science Policy (BELSPO) and Research Foundation - Flanders (FWO - Vlaanderen). FV, SG and KR thank FWO for financial support through the EOS-Excellence of Science program (ET-HoME - ID 30442502) and for providing the funding for the acquisition of the MC-ICP-MS instrumentation (ZW15-02 – G0H6216N). AMG and SM acknowledge support for nitrogen isotope analyses by the Max Planck Society. MZ acknowledges funding through the NWO VIDI project 016.161.365, which is financed by the Netherlands Organization for Scientific Research (NWO). XRF instrumentation at the VUB was funded by Hercules infrastructure grants. The authors would like to thank Bart Lippens for help with sample preparation, Arnold van Dijk for laboratory assistance, Wim Boer and Piet van Gaever for vital technical support, Eric Wagmaekers for maintaining the NIOZ jetty continuous measurements, the participants of the 2017 and 2018 edition of the NIOZ Marine Masters Summer School for their contribution to this research and Prof. Philippe Claeys for providing access to the X-Ray Fluorescence platform of the AMGC research group of the Vrije Universiteit Brussel for elemental analyses.

### APPENDIX A. SUPPLEMENTARY MATERIAL

Supplementary information is provided as a single PDF and can be found together with the supplementary data in the open-source online repository Zenodo (<http://www.doi.org/10.5281/zenodo.3904236>). Supplementary data to this article can be found online at <https://doi.org/10.1016/j.gca.2021.06.012>.

### REFERENCES

Addadi L., Joester D., Nudelman F. and Weiner S. (2006) Mollusk shell formation: a source of new concepts for understanding biomineralization processes. *Chem. – A Eur. J.* **12**, 980–987.

- Bajnai D., Fiebig J., Tomašových A., Milner Garcia S., Rollion-Bard C., Raddatz J., Löffler N., Primo-Ramos C. and Brand U. (2018) Assessing kinetic fractionation in brachiopod calcite using clumped isotopes. *Sci. Rep.* **8**, 1–12.
- Bajnai D., Guo W., Spötl C., Coplen T. B., Methner K., Löffler N., Krsnik E., Gischler E., Hansen M., Henkel D., Price G. D., Raddatz J., Scholz D. and Fiebig J. (2020) Dual clumped isotope thermometry resolves kinetic biases in carbonate formation temperatures. *Nat. Commun.* **11**, 1–9.
- Banker R. M. W. and Sumner D. Y. (2020) Structure and distribution of chalky deposits in the Pacific oyster using x-ray computed tomography (CT). *Sci. Rep.* **10**, 12118.
- Bernasconi S. M., Hu B., Wacker U., Fiebig J., Breitenbach S. F. and Rutz T. (2013) Background effects on Faraday collectors in gas-source mass spectrometry and implications for clumped isotope measurements. *Rapid Commun. Mass Spectrom.* **27**, 603–612.
- Bernasconi S. M., Müller I. A., Bergmann K. D., Breitenbach S. F., Fernandez A., Hodell D. A., Jaggi M., Meckler A. N., Millan I. and Ziegler M. (2018) Reducing uncertainties in carbonate clumped isotope analysis through consistent carbonate-based standardization. *Geochem. Geophys. Geosyst.* **19**, 2895–2914.
- Böttcher M. E., Brumsack H.-J. and Dürselen C.-D. (2007) The isotopic composition of modern seawater sulfate: I. Coastal waters with special regard to the North Sea. *J. Mar. Syst.* **67**, 73–82.
- Böttcher M. E., Oelschläger B., Höpner T., Brumsack H.-J. and Rullkötter J. (1998) Sulfate reduction related to the early diagenetic degradation of organic matter and “black spot” formation in tidal sandflats of the German Wadden Sea (southern North Sea): stable isotope ( $^{13}\text{C}$ ,  $^{34}\text{S}$ ,  $^{18}\text{O}$ ) and other geochemical results. *Org. Geochem.* **29**, 1517–1530.
- Bougeois L., de Rafélis M., Reichart G.-J., de Nooijer L. J., Nicollin F. and Dupont-Nivet G. (2014) A high resolution study of trace elements and stable isotopes in oyster shells to estimate Central Asian Middle Eocene seasonality. *Chem. Geol.* **363**, 200–212.
- Bougeois L., Dupont-Nivet G., De Rafélis M., Tindall J. C., Proust J.-N., Reichart G.-J., de Nooijer L. J., Guo Z. and Ormukov C. (2018) Asian monsoons and aridification response to Paleogene sea retreat and Neogene westerly shielding indicated by seasonality in Paratethys oysters. *Earth Planet. Sci. Lett.* **485**, 99–110.
- Bourbonnais A., Altabet M. A., Charoenpong C. N., Larkum J., Hu H., Bange H. W. and Stramma L. (2015) N-loss isotope effects in the Peru oxygen minimum zone studied using a mesoscale eddy as a natural tracer experiment. *Global Biogeochem. Cycles* **29**, 793–811.
- Bowen G. J. (2020) WaterIsotopes.org. Available at: <http://wateriso.utah.edu/waterisotopes/index.html> [Accessed July 28, 2020].
- Brunner B., Bernasconi S. M., Kleikemper J. and Schroth M. H. (2005) A model for oxygen and sulfur isotope fractionation in sulfate during bacterial sulfate reduction processes. *Geochim. Cosmochim. Acta* **69**, 4773–4785.
- Carré M., Bentaleb I., Bruguier O., Ordinola E., Barrett N. T. and Fontugne M. (2006) Calcification rate influence on trace element concentrations in aragonitic bivalve shells: Evidences and mechanisms. *Geochim. Cosmochim. Acta* **70**, 4906–4920.
- Carriker M. R. (1951) Ecological observations on the distribution of oyster larvae in New Jersey estuaries. *Ecol. Monogr.* **21**, 19–38.
- Carriker M. R., Palmer R. E. and Prezant R. S. (1980) Functional ultramorphology of the dissoconch valves of the oyster *Crasostrea virginica*. In Proceedings of the National Shellfisheries

- Association pp. 139–183. Available at: [https://www.researchgate.net/profile/Robert\\_Prezant2/publication/236964411\\_Functional\\_ultramorphology\\_of\\_the\\_dissoconch\\_valves\\_of\\_the\\_oyster\\_Crassostrea\\_virginica/links/53dfd2260cf2a768e49be892.pdf](https://www.researchgate.net/profile/Robert_Prezant2/publication/236964411_Functional_ultramorphology_of_the_dissoconch_valves_of_the_oyster_Crassostrea_virginica/links/53dfd2260cf2a768e49be892.pdf)
- Checa A. G., Esteban-Delgado F. J. and Rodríguez-Navarro A. B. (2007) Crystallographic structure of the foliated calcite of bivalves. *J. Struct. Biol.* **157**, 393–402.
- Checa A. G., Harper E. M. and González-Segura A. (2018) Structure and crystallography of foliated and chalk shell microstructures of the oyster *Magallana*: the same materials grown under different conditions. *Sci. Rep.* **8**, 1–12.
- Chinzei K. (1995) Adaptive significance of the lightweight shell structure in soft bottom oysters. *Neues Jahrbuch für Geologie und Paläontologie-Abhandlungen*, 217–227.
- Chinzei K. and Seilacher A. (1993) Remote biomineralization I. fill skeletons in vesicular oyster shells. *Neues Jahrbuch für Geologie und Paläontologie. Abhandlungen* **190**, 349–361.
- Cranford S. and Buehler M. J. (2010) Materiomics: biological protein materials, from nano to macro. *Nanotechnol., Sci. Appl.* **3**, 127.
- Daëron M., Blamart D., Peral M. and Afek H. P. (2016) Absolute isotopic abundance ratios and the accuracy of  $\Delta 47$  measurements. *Chem. Geol.* **442**, 83–96.
- Daëron M., Drysdale R. N., Peral M., Huyghe D., Blamart D., Copen T. B., Lartaud F. and Zanchetta G. (2019) Most Earth-surface calcites precipitate out of isotopic equilibrium. *Nat. Commun.* **10**, 429.
- Dähnke K., Emeis K., Johannsen A. and Nagel B. (2010) Stable isotope composition and turnover of nitrate in the German Bight. *Mar. Ecol. Prog. Ser.* **408**, 7–18.
- Dame R. F. (1999) Oyster reefs as components in estuarine nutrient cycling: Incidental or regulating. Oyster reef habitat restoration: a synopsis and synthesis of approaches. Edited by MW Luckenbach, R. Mann and JA Wesson. Virginia Institute of Marine Science Press, Gloucester Point, 267–280
- Dame R. F., Zingmark R. G. and Haskin E. (1984) Oyster reefs as processors of estuarine materials. *J. Exp. Mar. Biol. Ecol.* **83**, 239–247.
- Dauphin Y., Cuif J., Doucet J., Salomé M., Susini J. and Williams C. (2003) In situ mapping of growth lines in the calcitic prismatic layers of mollusc shells using X-ray absorption near-edge structure (XANES) spectroscopy at the sulphur K-edge. *Mar. Biol.* **142**, 299–304.
- Day C. C. and Henderson G. M. (2013) Controls on trace-element partitioning in cave-analogue calcite. *Geochim. Cosmochim. Acta* **120**, 612–627.
- Defliese W. F., Hren M. T. and Lohmann K. C. (2015) Compositional and temperature effects of phosphoric acid fractionation on  $\Delta 47$  analysis and implications for discrepant calibrations. *Chem. Geol.* **396**, 51–60.
- DeNiro M. J. and Epstein S. (1978) Influence of diet on the distribution of carbon isotopes in animals. *Geochim. Cosmochim. Acta* **42**, 495–506.
- de Winter N. J. and Claeys P. (2016) Micro X-ray fluorescence ( $\mu$ XRF) line scanning on Cretaceous rudist bivalves: A new method for reproducible trace element profiles in bivalve calcite ed. M. R. Petrizzo. *Sedimentology* **64**, 231–251.
- de Winter N. J., Goderis S., Dehairs F., Jagt J. W., Fraaije R. H., Van Malderen S. J., Vanhaecke F. and Claeys P. (2017a) Tropical seasonality in the late Campanian (late Cretaceous): Comparison between multiproxy records from three bivalve taxa from Oman. *Palaeogeogr. Palaeoclimatol. Palaeoecol.* **485**, 740–760.
- de Winter N. J., Sinnesael M., Makarona C., Vansteenberge S. and Claeys P. (2017b) Trace element analyses of carbonates using portable and micro-X-ray fluorescence: performance and optimization of measurement parameters and strategies. *J. Anal. At. Spectrom.* **32**, 1211–1223.
- de Winter N. J., Vellekoop J., Vorrsselmans R., Golreihan A., Soete J., Petersen Sierra V., Meyer Kyle W., Casadio S., Speijer Robert P. and Claeys P. (2018) An assessment of latest Cretaceous Pycnodonte vesicularis (Lamarck, 1806) shells as records for palaeoseasonality: a multi-proxy investigation. *Clim. Past* **14**, 725–749.
- de Winter Niels J., Ullmann C. V., Sørensen A. M., Thibault N., Goderis S., Van Malderen S. J. M., Snoeck C., Goolaerts S., Vanhaecke F. and Claeys P. (2020a) Shell chemistry of the boreal Campanian bivalve *Rastellum diluvianum*; (Linnaeus, 1767) reveals temperature seasonality, growth rates and life cycle of an extinct Cretaceous oyster. *Biogeosciences* **17**, 2897–2922.
- de Winter N., Agterhuis T. and Ziegler M. (2020) Optimizing sampling strategies in high-resolution paleoclimate records. *Climate of the Past Discussions*, 1–52.
- de Winter Niels J., Goderis S., Malderen S. J. M. V., Sinnesael M., Vansteenberge S., Snoeck C., Belza J., Vanhaecke F. and Claeys P. (2020d) Subdaily-Scale Chemical Variability in a Torreites Sanchezi Rudist Shell: Implications for Rudist Paleobiology and the Cretaceous Day-Night Cycle. *Paleoceanography and Paleoclimatology* **35**, e2019PA003723.
- Do Amaral V. S. and Simone L. R. L. (2014) Revision of genus *Crassostrea* (Bivalvia: Ostreidae) of Brazil. *J. Mar. Biol. Assoc. United Kingdom* **94**, 811–836.
- Dodd J. R. (1967) Magnesium and strontium in calcareous skeletons: a review. *J. Paleontol.* **41**, 1313–1329.
- Durham S. R., Gillikin D. P., Goodwin D. H. and Dietl G. P. (2017) Rapid determination of oyster lifespans and growth rates using LA-ICP-MS line scans of shell Mg/Ca ratios. *Palaeogeography, Palaeoclimatology, Palaeoecology*.
- England J., Cusack M. and Lee M. R. (2007) Magnesium and sulphur in the calcite shells of two brachiopods, *Terebratulina retusa* and *Novocrania anomala*. *Lethaia* **40**, 2–10.
- zu Ermgassen P. S. E., Spalding M. D., Grizzle R. E. and Brumbaugh R. D. (2013) Quantifying the Loss of a Marine Ecosystem Service: Filtration by the Eastern Oyster in US Estuaries. *Estuaries and Coasts* **36**, 36–43.
- Fisher R. A. (1932) *Statistical Methods for Research Workers*, 4th Edition. Oliver and Boyd, Edinburgh.
- Freitas P. S., Clarke L. J., Kennedy H., Richardson C. A. and Abrantes F. (2006) Environmental and biological controls on elemental (Mg/Ca, Sr/Ca and Mn/Ca) ratios in shells of the king scallop *Pecten maximus*. *Geochim. Cosmochim. Acta* **70**, 5119–5133.
- Gaetani G. A. and Cohen A. L. (2006) Element partitioning during precipitation of aragonite from seawater: a framework for understanding paleoproxies. *Geochim. Cosmochim. Acta* **70**, 4617–4634.
- Geerken E., de Nooijer L. J., Roepert A., Polerecky L., King H. E. and Reichart G. J. (2019) Element banding and organic linings within chamber walls of two benthic foraminifera. *Sci. Rep.* **9**, 3598.
- Gillikin D. P., Lorrain A., Jolivet A., Kelemen Z., Chauvaud L. and Bouillon S. (2017) High-resolution nitrogen stable isotope sclerochronology of bivalve shell carbonate-bound organics. *Geochim. Cosmochim. Acta* **200**, 55–66.
- Gillikin D. P., Lorrain A., Navez J., Taylor J. W., André L., Keppens E., Baeyens W. and Dehairs F. (2005) Strong biological controls on Sr/Ca ratios in aragonitic marine bivalve shells. *Geochem. Geophys. Geosyst.* **6**, Q05009.
- Goodwin D. H., Paul P. and Wissink C. L. (2009) MoGroFunGen: A numerical model for reconstructing intra-annual growth rates of bivalve molluscs. *Palaeogeogr. Palaeoclimatol. Palaeoecol.* **276**, 47–55.



- Goodwin D. H., Schöne B. R. and Dettman D. L. (2003) Resolution and fidelity of oxygen isotopes as paleotemperature proxies in bivalve mollusk shells: models and observations. *Palaios* **18**, 110–125.
- Grabowski J. H., Brumbaugh R. D., Conrad R. F., Keeler A. G., Opaluch J. J., Peterson C. H., Piehler M. F., Powers S. P. and Smyth A. R. (2012) Economic valuation of ecosystem services provided by oyster reefs. *Bioscience* **62**, 900–909.
- Grabowski J. H. and Peterson C. H. (2007) Restoring oyster reefs to recover ecosystem services. *Ecosystem Engineers: Plants to Protists* **4**, 281–298.
- Graniero L. E., Gillikin D. P., Surge D., Kelemen Z. and Bouillon S. (2021) Assessing  $\delta^{15}\text{N}$  values in the carbonate-bound organic matrix and periostracum of bivalve shells as environmental archives. *Palaeogeogr. Palaeoclimatol. Palaeoecol.* **564** 110108.
- Gray J. E. (1833) Some observations on the economy of molluscous animals, and the structure of their shells. *Philos. Trans. R. Soc. Lond.* **123**, 771–819.
- Hagiwara S. and Byerly L. (1981) Calcium channel. *Annu. Rev. Neurosci.* **4**, 69–125.
- Harding J. M. and Mann R. (2006) Age and growth of wild suminoe (*Crassostrea ariakensis*, Fugita 1913) and Pacific (C. *Gigas*, Thunberg 1793) oysters from Laizhou bay, China. *J. Shellfish Res.* **25**, 73–82.
- Harwood A. J. P., Dennis P. F., Marca A. D., Pilling G. M. and Millner R. S. (2008) The oxygen isotope composition of water masses within the North Sea. *Estuar. Coast. Shelf Sci.* **78**, 353–359.
- Harzhauser M., Piller W. E., Müllegger S., Grunert P. and Micheels A. (2011) Changing seasonality patterns in Central Europe from Miocene Climate Optimum to Miocene Climate Transition deduced from the *Crassostrea* isotope archive. *Global Planet. Change* **76**, 77–84.
- Hauzer H., Evans D., Müller W., Rosenthal Y. and Erez J. (2018) Calibration of Na partitioning in the calcitic foraminifer *Operculina ammonoides* under variable Ca concentration: Toward reconstructing past seawater composition. *Earth Planet. Sci. Lett.* **497**, 80–91.
- Higuera-Ruiz R. and Elorza J. (2009) Biometric, microstructural, and high-resolution trace element studies in *Crassostrea gigas* of Cantabria (Bay of Biscay, Spain): Anthropogenic and seasonal influences. *Estuar. Coast. Shelf Sci.* **82**, 201–213.
- Höche N., Peharda M., Walliser E. O. and Schöne B. R. (2020) Morphological variations of crossed-lamellar ultrastructures of *Glycymeris bimaculata* (Bivalvia) serve as a marine temperature proxy. *Estuar. Coast. Shelf Sci.* **237** 106658.
- Huber M. (2010) Compendium of bivalves. A full-color guide to 3,300 of the world's marine bivalves. A status on Bivalvia after 250 years of research., ConchBooks.
- Huyghe D., de Raféls M., Ropert M., Mouchi V., Emmanuel L., Renard M. and Lartaud F. (2019) New insights into oyster high-resolution hinge growth patterns. *Mar. Biol.* **166**, 48.
- IAEA/WMO (2015) Global Network of Isotopes in Precipitation. The GNIP Database. Available at: <https://nucleus.iaea.org/wiser/index.aspx> [Accessed July 28, 2020].
- Ichikuni M. (1983) Anionic substitution in calcium carbonate. In: *The Significance of Trace Elements in Solving Petrogenetic Problems and Controversies* (ed. S. S. Augustithis), pp. 83–94.
- Jia L., Cai C., Yang H., Li H., Wang T., Zhang B., Jiang L. and Tao X. (2015) Thermochemical and bacterial sulfate reduction in the Cambrian and Lower Ordovician carbonates in the Tazhong A rea, Tarim Basin, NW China: evidence from fluid inclusions, C, S, and S r isotopic data. *Geofluids* **15**, 421–437.
- Jones D. S. (1983) Sclerochronology: reading the record of the molluscan shell: annual growth increments in the shells of bivalve molluscs record marine climatic changes and reveal surprising longevity. *Am. Sci.* **71**, 384–391.
- Judd, J., Emil et al. (2020) A Dynamical Framework for Interpreting Ancient Sea Surface Temperatures. *Geophysical Research Letters* **47**(15) e2020GL089044.
- Judd E. J., Wilkinson B. H. and Ivany L. C. (2018) The life and time of clams: Derivation of intra-annual growth rates from high-resolution oxygen isotope profiles. *Palaeogeogr. Palaeoclimatol. Palaeoecol.* **490**, 70–83.
- Kele S., Breitenbach S. F., Capezzuoli E., Meckler A. N., Ziegler M., Millan I. M., Kluge T., Deák J., Hanselmann K. and John C. M. (2015) Temperature dependence of oxygen-and clumped isotope fractionation in carbonates: a study of travertines and tufas in the 6–95 C temperature range. *Geochim. Cosmochim. Acta* **168**, 172–192.
- Kennedy V. S., Newell R. I. and Eble A. F. (1996) The eastern oyster: *Crassostrea virginica*., University of Maryland Sea Grant College.
- Kim S.-T. and O'Neil J. R. (1997) Equilibrium and nonequilibrium oxygen isotope effects in synthetic carbonates. *Geochim. Cosmochim. Acta* **61**, 3461–3475.
- Kirby M. X., Soniat T. M. and Spero H. J. (1998) Stable isotope sclerochronology of Pleistocene and Recent oyster shells (*Crassostrea virginica*). *Palaios* **13**, 560–569.
- Kitano Y., Okumura M. and Idogaki M. (1975) Incorporation of sodium, chloride and sulfate with calcium carbonate. *Geochem. J.* **9**, 75–84.
- Klein R. T., Lohmann K. C. and Thayer C. W. (1996) Sr/Ca and  $^{13}\text{C}/^{12}\text{C}$  ratios in skeletal calcite of *Mytilus trossulus*: Covariation with metabolic rate, salinity, and carbon isotopic composition of seawater. *Geochim. Cosmochim. Acta* **60**, 4207–4221.
- Kocken I. J., Müller I. A. and Ziegler M. (2019) Optimizing the use of carbonate standards to minimize uncertainties in clumped isotope data. *Geochem. Geophys. Geosyst.* **20**, 5565–5577.
- Korringa P. (1951) On the nature and function of “chalky” deposits in the shell of *Ostrea edulis* Linnaeus. *Proc. Calif. Acad. Sci.* **27**, 133–158.
- Lartaud F., Emmanuel L., De Raféls M., Ropert M., Labourdette N., Richardson C. A. and Renard M. (2010a) A latitudinal gradient of seasonal temperature variation recorded in oyster shells from the coastal waters of France and The Netherlands. *Facies* **56**, 13.
- Lartaud F., De Raféls M., Ropert M., Emmanuel L., Geairon P. and Renard M. (2010b) Mn labelling of living oysters: artificial and natural cathodoluminescence analyses as a tool for age and growth rate determination of C. *gigas* (Thunberg, 1793) shells. *Aquaculture* **300**, 206–217.
- Lee S.-W., Jang Y.-N., Ryu K.-W., Chae S.-C., Lee Y.-H. and Jeon C.-W. (2011) Mechanical characteristics and morphological effect of complex crossed structure in biomaterials: fracture mechanics and microstructure of chalky layer in oyster shell. *Micron* **42**, 60–70.
- Leichtler J. N., Lüdecke T., Foreman A. D., Duprey N. N., Winkler D. E., Kast E. R., Vonhof H., Sigman D. M., Haug G. H., Clauss M., Tütken T. and Martínez-García A. (2021) Nitrogen isotopes in tooth enamel record diet and trophic level enrichment: Results from a controlled feeding experiment. *Chem. Geol.* **563** 120047.
- Lorens R. B. (1981) Sr, Cd, Mn and Co distribution coefficients in calcite as a function of calcite precipitation rate. *Geochim. Cosmochim. Acta* **45**, 553–561.
- Lorens R. B. and Bender M. L. (1980) The impact of solution chemistry on *Mytilus edulis* calcite and aragonite. *Geochim. Cosmochim. Acta* **44**, 1265–1278.
- Lorrain A., Gillikin D. P., Paulet Y.-M., Chauvaud L., Le Mercier A., Navez J. and André L. (2005) Strong kinetic effects on Sr/

- Ca ratios in the calcitic bivalve *Pecten maximus*. *Geology* **33**, 965–968.
- Lueders-Dumont J. A., Wang X. T., Jensen O. P., Sigman D. M. and Ward B. B. (2018) Nitrogen isotopic analysis of carbonate-bound organic matter in modern and fossil fish otoliths. *Geochim. Cosmochim. Acta* **224**, 200–222.
- Luz G. M. and Mano J. F. (2010) Mineralized structures in nature: Examples and inspirations for the design of new composite materials and biomaterials. *Compos. Sci. Technol.* **70**, 1777–1788.
- Malone M. J. and Baker P. A. (1999) Temperature dependence of the strontium distribution coefficient in calcite; an experimental study from 408 degrees to 2008 degrees C and application to natural diagenetic calcites. *J. Sediment. Res.* **69**, 216–223.
- McConnaughey T. A. and Gillikin D. P. (2008) Carbon isotopes in mollusk shell carbonates. *Geo-Mar. Lett.* **28**, 287–299.
- McGenity T. J. and Sellwood B. W. (1999) New approaches to studying the microbial precipitation of carbonate minerals. *Sed. Geol.* **126**, 5–8.
- Meckler A. N., Ziegler M., Millán M. I., Breitenbach S. F. and Bernasconi S. M. (2014) Long-term performance of the Kiel carbonate device with a new correction scheme for clumped isotope measurements. *Rapid Commun. Mass Spectrom.* **28**, 1705–1715.
- Mook W. G. (1970) Stable carbon and oxygen isotopes of natural waters in the Netherlands. *Isotope Hydrology* **1970**, 163–190.
- Morse J. W. and Bender M. L. (1990) Partition coefficients in calcite: Examination of factors influencing the validity of experimental results and their application to natural systems. *Chem. Geol.* **82**, 265–277.
- Mouchi V., De Rafélis M., Lartaud F., Fialin M. and Verrecchia E. (2013) Chemical labelling of oyster shells used for time-calibrated high-resolution Mg/Ca ratios: a tool for estimation of past seasonal temperature variations. *Palaeogeogr. Palaeoclimatol. Palaeoecol.* **373**, 66–74.
- Mouchi V., Lartaud F., Guichard N., Immel F., de Rafélis M., Broussard C., Crowley Q. G. and Marin F. (2016) Chalky versus foliated: a discriminant immunogold labelling of shell microstructures in the edible oyster *Crassostrea gigas*. *Mar. Biol.* **163**, 256.
- Murray S. T., Arienzo M. M. and Swart P. K. (2016) Determining the  $\Delta 47$  acid fractionation in dolomites. *Geochim. Cosmochim. Acta* **174**, 42–53.
- Newell R. I. (1988) Ecological changes in Chesapeake Bay: are they the result of overharvesting the American oyster, *Crassostrea virginica*. *Understanding the Estuary: Advances in Chesapeake Bay Research* **129**, 536–546.
- Onuma N., Masuda F., Hirano M. and Wada K. (1979) Crystal structure control on trace element partition in molluscan shell formation. *Geochem. J.* **13**, 187–189.
- Owen R., Kennedy H. and Richardson C. (2002) Isotopic partitioning between scallop shell calcite and seawater: effect of shell growth rate. *Geochim. Cosmochim. Acta* **66**, 1727–1737.
- Paris G., Sessions A. L., Subhas A. V. and Adkins J. F. (2013) MC-ICP-MS measurement of  $\delta 34S$  and  $\Delta 33S$  in small amounts of dissolved sulfate. *Chem. Geol.* **345**, 50–61.
- Pätsch J., Serna A., Dähnke K., Schlarbaum T., Johannsen A. and Emeis K.-C. (2010) Nitrogen cycling in the German Bight (SE North Sea) — Clues from modelling stable nitrogen isotopes. *Cont. Shelf Res.* **30**, 203–213.
- Pilson M. E. (2012) *An Introduction to the Chemistry of the Sea*. Cambridge University Press.
- Pracht H., Metcalfe B. and Peeters F. J. C. (2018) Oxygen isotope composition of final chamber of planktic foraminifera provides evidence for vertical migration and depth integrated growth., *Paleobiogeoscience: Proxy use, Development & Validation*. Available at: <https://www.biogeosciences-discuss.net/bg-2018-146/bg-2018-146.pdf> [Accessed June 9, 2020].
- Ren H., Sigman D. M., Meckler A. N., Plessen B., Robinson R. S., Rosenthal Y. and Haug G. H. (2009) Foraminiferal isotope evidence of reduced nitrogen fixation in the ice age Atlantic Ocean. *Science* **323**, 244–248.
- Rennie V. C., Paris G., Sessions A. L., Abramovich S., Turchyn A. V. and Adkins J. F. (2018) Cenozoic record of  $\delta 34S$  in foraminiferal calcite implies an early Eocene shift to deep-ocean sulfide burial. *Nat. Geosci.* **11**, 761–765.
- Richardson C. A., Collis S. A., Ekaratne K., Dare P. and Key D. (1993) The age determination and growth rate of the European flat oyster, *Ostrea edulis*, in British waters determined from acetate peels of umbo growth lines. *ICES J. Mar. Sci.* **50**, 493–500.
- Richardson J. A., Newville M., Lanzirotti A., Webb S. M., Rose C. V., Catalano J. G. and Fike D. A. (2019) The source of sulfate in brachiopod calcite: Insights from  $\mu$ -XRF imaging and XANES spectroscopy. *Chem. Geol.* **529** 119328.
- Rimstidt J. D., Balog A. and Webb J. (1998) Distribution of trace elements between carbonate minerals and aqueous solutions. *Geochim. Cosmochim. Acta* **62**, 1851–1863.
- Rolf C., Elmgren R. and Voss M. (2008) Deposition of nitrogen and phosphorus on the Baltic Sea: seasonal patterns and nitrogen isotope composition. *Biogeosci. Discuss.*, 5.
- Salomons W. and Mook W. G. (1981) Field observations of the isotopic composition of particulate organic carbon in the southern North Sea and adjacent estuaries. *Mar. Geol.* **41**, M11–M20.
- Schindelin J., Arganda-Carreras I., Frise E., Kaynig V., Longair M., Pietzsch T., Preibisch S., Rueden C., Saalfeld S. and Schmid B. (2012) Fiji: an open-source platform for biological-image analysis. *Nat. Methods* **9**, 676–682.
- Schoeninger M. J. and DeNiro M. J. (1984) Nitrogen and carbon isotopic composition of bone collagen from marine and terrestrial animals. *Geochim. Cosmochim. Acta* **48**, 625–639.
- Schöne B. R., Dunca E., Fiebig J. and Pfeiffer M. (2005a) Mutvei's solution: An ideal agent for resolving microgrowth structures of biogenic carbonates. *Palaeogeogr. Palaeoclimatol. Palaeoecol.* **228**, 149–166.
- Schöne B. R., Houk S. D., Castro A. D. F., Fiebig J., Oschmann W., Kröncke I., Dreyer W. and Gosseck F. (2005b) Daily growth rates in shells of *Arctica islandica*: assessing sub-seasonal environmental controls on a long-lived bivalve mollusk. *Palaaios* **20**, 78–92.
- Schöne B. R., Zhang Z., Jacob D., Gillikin D. P., Tütken T., Garbe-Schönberg D., McConnaughey T. and Soldati A. (2010) Effect of organic matrices on the determination of the trace element chemistry (Mg, Sr, Mg/Ca, Sr/Ca) of aragonitic bivalve shells (*Arctica islandica*)—Comparison of ICP-OES and LA-ICP-MS data. *Geochem. J.* **44**, 23–37.
- Schöne B. R., Zhang Z., Radermacher P., Thébault J., Jacob D. E., Nunn E. V. and Maurer A.-F. (2011) Sr/Ca and Mg/Ca ratios of ontogenetically old, long-lived bivalve shells (*Arctica islandica*) and their function as paleotemperature proxies. *Palaeogeogr. Palaeoclimatol. Palaeoecol.* **302**, 52–64.
- Scyphers S. B., Powers S. P., Heck Jr K. L. and Byron D. (2011) Oyster reefs as natural breakwaters mitigate shoreline loss and facilitate fisheries. *PloS one* **6**.
- Sigman D. M., Casciotti K. L., Andreani M., Barford C., Galanter M. and Böhlke J. K. (2001) A bacterial method for the nitrogen isotopic analysis of nitrate in seawater and freshwater. *Anal. Chem.* **73**, 4145–4153.
- Stenzel H. B. (1971) Oysters. *Treatise on Invertebrate Paleontology, Part N, Bivalvia* **3**, N953–N1224.

- Stoll H. M., Klaas C. M., Probert I., Encinar J. R. and Garcia Alonso J. I. (2002) Calcification rate and temperature effects on Sr partitioning in coccoliths of multiple species of coccolithophorids in culture. *Global and Planetary Change* **34**, 153–171.
- Straub M., Sigman D. M., Ren H., Martínez-García A., Meckler A. N., Hain M. P. and Haug G. H. (2013) Changes in North Atlantic nitrogen fixation controlled by ocean circulation. *Nature* **501**, 200–203.
- Stribling J. M. and Cornwell J. C. (1997) Identification of important primary producers in a Chesapeake Bay tidal creek system using stable isotopes of carbon and sulfur. *Estuaries* **20**, 77–85.
- Surge D. and Lohmann K. C. (2008) Evaluating Mg/Ca ratios as a temperature proxy in the estuarine oyster, *Crassostrea virginica*. *J. Geophys. Res.* **113**, G02001.
- Surge D., Lohmann K. C. and Dettman D. L. (2001) Controls on isotopic chemistry of the American oyster, *Crassostrea virginica*: implications for growth patterns. *Palaeogeogr. Palaeoclimatol. Palaeoecol.* **172**, 283–296.
- Takesue R. K., Bacon C. R. and Thompson J. K. (2008) Influences of organic matter and calcification rate on trace elements in aragonitic estuarine bivalve shells. *Geochim. Cosmochim. Acta* **72**, 5431–5445.
- Tang J., Köhler S. J. and Dietzel M. (2008) Sr<sup>2+</sup>/Ca<sup>2+</sup> and 44Ca/40Ca fractionation during inorganic calcite formation: I. Sr incorporation. *Geochim. Cosmochim. Acta* **72**, 3718–3732.
- Terakado Y., Ofuka Y. and Tada N. (2010) Rare earth elements, Sr, Ba, Fe, and major cation concentrations in some living foraminiferal tests collected from Iriomote Island, Japan: An exploration for trace element behavior during biogenic calcium carbonate formation. *Geochem. J.* **44**, 315–322.
- Thunberg C. (1793) Teckning och beskrifning pa en stor Ostronsort ifran Japan. K. Svenska Vetenskapsakademien, Handlinger.
- Trofimova T., Milano S., Andersson C., Bonitz F. G. W. and Schöne B. R. (2018) Oxygen Isotope Composition of Arctica islandica Aragonite in the Context of Shell Architectural Organization: Implications for Paleoclimate Reconstructions. *Geochem. Geophys. Geosyst.* **19**, 453–470.
- Tynan S., Opdyke B. N., Walczak M., Eggins S. and Dutton A. (2017) Assessment of Mg/Ca in *Saccostrea glomerata* (the Sydney rock oyster) shell as a potential temperature record. *Palaeogeogr. Palaeoclimatol. Palaeoecol.* **484**, 79–88.
- Ullmann C. V., Böhm F., Rickaby R. E. M., Wiechert U. and Korte C. (2013) The Giant Pacific Oyster (*Crassostrea gigas*) as a modern analog for fossil ostreoids: Isotopic (Ca, O, C) and elemental (Mg/Ca, Sr/Ca, Mn/Ca) proxies. *Geochem. Geophys. Geosyst.* **14**, 4109–4120.
- Ullmann C. V., Wiechert U. and Korte C. (2010) Oxygen isotope fluctuations in a modern North Sea oyster (*Crassostrea gigas*) compared with annual variations in seawater temperature: Implications for palaeoclimate studies. *Chem. Geol.* **277**, 160–166.
- van Dijk I., de Nooijer L. J., Boer W. and Reichart G.-J. (2017) Sulfur in foraminiferal calcite as a potential proxy for seawater carbonate ion concentration. *Earth Planet. Sci. Lett.* **470**, 64–72.
- van Hulten M. M. P., Middag R., Dutay J.-C., de Baar H. J. W., Roy-Barman M., Gehlen M., Tagliabue A. and Sterl A. (2016) Manganese in the West Atlantic Ocean in context of the first global ocean circulation model of manganese. arXiv preprint arXiv:1606.07128.
- Vermeij G. J. (2014) The oyster enigma variations: a hypothesis of microbial calcification. *Paleobiology* **40**, 1–13.
- Voss M., Liskow I., Pastuszek M., Rüb D., Schulte U. and Dippner J. W. (2005) Riverine discharge into a coastal bay: A stable isotope study in the Gulf of Gdańsk, Baltic Sea. *J. Mar. Syst.* **57**, 127–145.
- Wanamaker, Jr, A. D., Kreutz K. J., Wilson T., Borns, Jr, H. W., Introne D. S. and Feindel S. (2008) Experimentally determined Mg/Ca and Sr/Ca ratios in juvenile bivalve calcite for *Mytilus edulis*: implications for paleotemperature reconstructions. *Geo-Mar. Lett.* **28**, 359–368.
- Wang X. T., Prokopenko M. G., Sigman D. M., Adkins J. F., Robinson L. F., Ren H., Oleynik S., Williams B. and Haug G. H. (2014) Isotopic composition of carbonate-bound organic nitrogen in deep-sea scleractinian corals: A new window into past biogeochemical change. *Earth Planet. Sci. Lett.* **400**, 243–250.
- Wang X. T., Sigman D. M., Cohen A. L., Sinclair D. J., Sherrell R. M., Cobb K. M., Erler D. V., Stolarski J., Kitahara M. V. and Ren H. (2016) Influence of open ocean nitrogen supply on the skeletal  $\delta^{15}\text{N}$  of modern shallow-water scleractinian corals. *Earth Planet. Sci. Lett.* **441**, 125–132.
- Watson E. B. and Liang Y. (1995) A simple model for sector zoning in slowly grown crystals: Implications for growth rate and lattice diffusion, with emphasis on accessory minerals in crustal rocks. *Am. Mineral.* **80**, 1179–1187.
- Webb G. E. and Kamber B. S. (2000) Rare earth elements in Holocene reefal microbialites: a new shallow seawater proxy. *Geochim. Cosmochim. Acta* **64**, 1557–1565.
- Weigand M. A., Foriel J., Barnett B., Oleynik S. and Sigman D. M. (2016) Updates to instrumentation and protocols for isotopic analysis of nitrate by the denitrifier method. *Rapid Commun. Mass Spectrom.* **30**, 1365–1383.
- Wilkinson B. H. and Ivany L. C. (2002) Paleoclimatic inference from stable isotope profiles of accretionary biogenic hardparts – a quantitative approach to the evaluation of incomplete data. *Palaeogeogr. Palaeoclimatol. Palaeoecol.* **185**, 95–114.
- Witbaard R., Jenness M. I., Van Der Borg K. and Ganssen G. (1994) Verification of annual growth increments in *Arctica islandica* L. from the North Sea by means of oxygen and carbon isotopes. *Neth. J. Sea Res.* **33**, 91–101.
- Yonge C. M. (1960) The New Naturalist Special Volume-Oysters. Yoon G.-L., Kim B.-T., Kim B.-O. and Han S.-H. (2003) Chemical–mechanical characteristics of crushed oyster-shell. *Waste Manage.* **23**, 825–834.

Associate editor: Heather Stoll